Experimental and numerical comparative study on the crashworthiness of pristine and recycled fiber-reinforced polymeric 3D-printed lattice structures

Thin–Walled Structures 226 (2026) 114902

Contents lists available at ScienceDirect

Thin-Walled Structures

journal homepage: www.elsevier.com/locate/tws

Full length article

Experimental and numerical comparative study on the crashworthiness of pristine and recycled fiber-reinforced polymeric 3D-printed lattice structures

Francesco Bandinelli *, Lorenzo Peroni, Martina Scapin

Politecnico di Torino, Department of Mechanical and Aerospace Engineering, Corso Duca degli Abruzzi, 24, 10129 Turin, Italy

ARTICLE INFO

Keywords:
Crashworthiness
Hopkinson Bar
Lattice structure
Additive manufacturing
3D-printed
Fiber reinforced polymer
Energy absorption
High speed testing

ABSTRACT

The energy absorption performance of 3D-printed polymeric lattice structures has been recently studied extensively. Different structures, built with different additive manufacturing techniques, have been tested in both quasi-static and dynamic conditions. Recycled plastics are being introduced into the additive manufacturing sector, but research on engineering components that can address their peculiar characteristics is lacking. In this work, 3D-printed closed-cell lattice structures are fabricated using a short fiber reinforced polyamide, both in its pristine and recycled form. Two different printing techniques are used to compare two possible scenarios: printing from filament pristine material and printing from shredded waste of the same material. A direct impact Hopkinson pressure bar setup is used to test the dynamic energy absorption properties of cellular structures with three different overall densities of the same infill geometry. A wave separation technique based on deconvolution is employed to limit the length of the output bar. The dynamic energy absorption performances are compared with the quasi-static ones, observing two different behaviors for pristine and recycled specimens. Quantitatively, the pristine material resulted in an increase of up to 22% in SEA in dynamic conditions, while the recycled one resulted in a decrease of up to 25% in the same conditions. The recycled material had an average 7.8% higher SEA in quasi-static conditions, while it showed an average 25.4% lower SEA in dynamic conditions, compared to the pristine material. Finally, anisotropic finite element models are developed, representing the dynamic behavior of the specimens, proving to be accurate design and verification tools.

1. Introduction

In recent years, much attention has been paid to 3D-printed structures for crash-absorbing applications. Thanks to additive manufacturing techniques, lattice structures are now utilized in various engineering components to leverage their high specific mechanical properties [1–3]. Among possible applications, crash-absorbing components have been recently investigated as a viable way to employ these structures [4–6]. Properties such as lightweight, high specific strength, and the ability to tune almost endless mechanical properties make these structures suitable for such applications. Lattice structures for crash-absorbing applications are usually realized by metallic or polymeric materials due to their ability to withstand plastic deformation. The first ones allow maximum mechanical properties, but require high costs for both materials and production techniques. The second ones are promising substitutes since they can reach interesting specific mechanical properties, but at only a fraction of the cost.

Recently, many researchers have investigated the mechanical properties of lattice structures, mainly focusing on their quasi-static compression performance [7–9]. Other researchers have focused on the high-speed testing and crashworthiness evaluation of lattice structures, observing some differences from the quasi-static behavior [10–12]. The influence of the strain rate on the mechanical properties and energy absorption performance of these structures has often been shown to be non-negligible. Calladine and English investigated the strain rate and inertia effects on the collapse of energy-absorbing structures, dividing them into two categories [13]. They observed that lateral inertial effects, acting when thin walls are subjected to buckling at high speeds, are highly influential on their energy-absorbing behavior. Elnasri et al. observed the shock behavior of cellular structures under impact loading, studying the impact performance of aluminum foams and honeycombs at a speed of around 50 m/s [14].

* Corresponding author.
E-mail address: francesco.bandinelli@polito.it (F. Bandinelli).

https://doi.org/10.1016/j.tws.2026.114902
Received 20 January 2026; Received in revised form 30 March 2026; Accepted 30 March 2026
Available online 2 April 2026

They found that aluminum specimens, although generally considered as a strain rate insensitive material, showed an increase of initial stress levels of up to 60% for Alporas foams and nickel hollow spheres agglomerates when tested at 55 m/s. It is then important to investigate the high strain rate behavior of 3D-printed lattice structures to ensure a relevant evaluation of their mechanical properties in the proper working conditions. Up to now, a number of studies have investigated the strain rate dependency of such structures, showing that different behaviors are obtained when testing such structures in quasi-static and dynamic conditions. Bouteldja et al. [5] studied the quasi-static and dynamic compression behavior of lattice ABS and tough-PLA 3D-printed structures, using drop-weight tests at a speed of 4 m/s. They observed a clearly different mechanical behavior of the same structure in the two loading conditions: a more ductile behavior was observed in the quasi-static regime, while a brittle behavior was observed in the dynamic compression regime. Furthermore, depending on the structure, notable decreases were observed in the energy absorbed during the tests, showing a clear strain rate dependency of the materials' properties. Feng et al. [11] investigated both the quasi-static and dynamic behavior of functionally graded TPMS structures made of PLA, also performing numerical simulations of the tests. They found that the structures have strain-rate-dependent mechanical properties, with the effect of loading speed depending on the relative densities of the structures. Lower relative densities (20%) suffered from more extended fracture behavior, thus showing less energy absorption capability compared to their quasi-static counterparts. Higher relative densities (40%) showed an increase in energy absorption up to 62.4% reaching a specific energy absorption (SEA) value of 11.22 J/g. A Cowper-Symonds isotropic numerical model was employed to represent the 3D-printed material behavior in the finite element analysis. Almahri et al. [12] studied the quasi-static and dynamic mechanical properties of metallic TPMS structures using a Direct Impact Hopkinson Pressure Bar (DIHPB) setup. They observed a relevant increase in SEA for all the structures analyzed, with values of 30.85 J/g and 35.57 J/g for the diamond structure in quasi-static and dynamic testing conditions, respectively. The strain rate was varied from 0.005 s^{-1} in the quasi-static case to 2057 s^{-1} in the dynamic experiments.

Based on the results from the current literature, lattice structures are promising candidates to substitute other conventional solutions for crash mitigation purposes in high-speed impact scenarios. In the field of finite element analysis, 3D-printed structures are generally represented by isotropic material models, thus limiting the accuracy of the simulations. Abueidda et al. [15] investigated the behavior of gyroid PLA specimens, simulating their behavior using an Arruda-Boyce model, which is an isotropic material model. Although obtaining a good representation of the elastic moduli of the structures, the same cannot be assessed for the deformation prediction. Nam et al. [16] investigated the quasi-static behavior of 3D-printed octet plate-lattices, and simulated their compression behavior using an isotropic material model. Deformation behavior and load response were reproduced, but the experimental case was sufficiently guided by density gradients and the geometry of the structure. In more generic simulations, the use of isotropic material models may not be sufficient to describe the behavior of the lattices. For example, Feng et al. [11] simulated the behavior of TPMS PLA structures using an isotropic material model, which resulted in limited predictive capability, depending on the structure type. Until now, only a few studies have focused on the finite element modelling of the crushing behavior of 3D-printed structures. Most studies employ isotropic material models, which are often unable to capture the collapse behavior of the complex structures [16–18]. The anisotropic nature of the 3D-printed material is particularly evident for thin-walled lattices made of polymeric materials, where the small thickness of the walls enhances the overall anisotropy [19]. The intrinsic anisotropy of FFF printed materials is often neglected when simulating the mechanical behavior of 3D-printed structures, while it may play a substantial role in defining the overall mechanical performance of such components.

Increasing attention is given to the sustainability of engineering products and processes, since pollution and increasing energy demand are global key challenges to be tackled in the upcoming years. Plastic production and disposal are among the main concerns of our times, since they involve both high consumption of resources and severe pollution [20]. In this context, plastic additive manufacturing processes must take into account the possibility of including recycled polymers as raw materials [21,22]. Based on this premise, many studies have lately investigated the use of recycled plastics as new materials for additive manufacturing processes. Sanchez et al. [23] investigated the mechanical behavior of 3D-printed recycled PLA, observing a decrease in almost every relevant mechanical property. They also observed an improved flowability of the polymeric fused material, with consequent reduced porosity of the printed parts. Spirio et al. [24] studied the possibility of using e-waste (plastic waste recovered from electric and electronic apparatus) as a new source for 3D printing filaments, proving successful 3D printing with PP waste. Walker et al. [25] recovered machined flakes from the milling process of a 3D-printed composite component to study the mechanical properties of recycled 3D-printed specimens via big area additive manufacturing. They observed a significant reduction in fiber length, with a consequent loss in mechanical properties. Interestingly, the ultimate tensile strength in the vertical printing direction was higher in recycled specimens. This was explained by the improved adhesion due to the improved flowability of the polymeric matrix, observed after major fiber length reduction. While significant progress has been made in the evaluation of the mechanical properties of recycled 3D-printed materials, research is still lacking on the study of functional components. Ma et al. [26] built an optimization framework to select the best printing parameters based on recycled PLA to maximize the mechanical performance of lattice structures. They proved that changing the printing parameters from those prescribed for the pristine material could improve the strength of the final components up to 23%. In a previous work [27], the authors investigated the recycling process and Fused Granular Fabrication (FGF) 3D printing of short carbon fiber reinforced PA12, both by tensile specimens and a lattice core sandwich structure. They compared pristine and recycled material, observing relevant differences: tensile specimens showed comparable mechanical properties to those of pristine ones; on the other hand, recycled sandwich lattice core panels proved to be less effective than pristine ones. This was because recycled material exhibited a higher density, which forced the lattice structure to have a lower geometric density in order to obtain the same weight. This finally led to a lower energy-absorbing performance, proving that lattice structures in particular need extended work to evaluate their performance when built using recycled materials. Byard et al. [28] investigated the economic aspects of using recycled ABS and PP to 3D print functional components as kayak paddles, skateboards, and snowshoes. They successfully printed the final components, showing both the functionality of the products and their economic advantage compared to conventional production solutions. To the best of the authors' knowledge, only a few studies have investigated the use of recycled polymers in additive manufacturing processes to fabricate functional engineering components. However, this is a key aspect to prove the possibility of using recycled polymers as a viable substitute for pristine ones.

In this study, FFF and FGF 3D printing techniques are used to fabricate lattice components for crash-absorbing purposes, using both pristine and recycled carbon fiber reinforced PA12. This material is chosen for its high specific mechanical performances shown in previous works by the authors and for its proven ability to withstand shock loads. The polymeric ductile matrix provides sufficient toughness, while short carbon fibers improve mechanical resistance. To the best of the authors' knowledge, no study has investigated the crashworthiness of lattice structures built with recycled materials, which is fundamental for the development of such sustainable engineering solutions. The aim of the work is to assess the behavior of protective 3D-printed lattice structures in both quasi-static and dynamic loading conditions, examining the technological solutions of FFF and FGF 3D printing with pristine and recycled material, respectively. A thorough analysis of 3D-printed structures in dynamic conditions is needed to properly assess their behavior in real operating conditions, which is not often accomplished by common research works. The dynamic behavior of 3D-printed structures is often investigated in quasi-static conditions only, and the effects of material recycling on the engineering performance of such structures are still to be clearly identified. Cubic lattice structures with three different overall densities (200 g/l, 300 g/l, and 400 g/l) are fabricated so that a wide range of densities is studied and compared to similar engineering solutions. Two different printing technologies are employed to compare two different technical solutions, rather than comparing the same material in pristine and recycled forms. Quasi-static and high-speed impact compression tests are conducted to evaluate their mechanical behavior and to compare the two materials. A DIHPB apparatus with high-speed cameras and linescan cameras is developed, using wave separation techniques to derive the load-displacement curves of the tested specimens. This allows the accurate crashworthiness evaluation of these structures, overcoming the limits of common testing methods. Many studies have already highlighted relevant differences between the quasi-static and dynamic behavior of 3D-printed lattice structures. The precise evaluation of the lattices' mechanical properties under high strain rate conditions is crucial to the understanding of their possible use in high-speed impact scenarios. Ultimately, finite element models are developed to simulate the behavior of both pristine and recycled specimens, using an anisotropic material model and full-scale geometry models.

2. Materials and experimental methods

2.1. 3D printing of specimens

Two different 3D printing techniques are employed to fabricate the infill lattice structures: fused filament fabrication (FFF) and fused granular fabrication (FGF). The first one uses the raw material in a filament form, the most common commercially available; the second one allows printing from pellets or shredded flakes, which allows a wider material selection, including raw recycled materials. In this work, the comparison is on the two technological solutions rather than on the recycled and pristine material conditions, which have already been investigated in a past work by the authors [27]. For the FFF 3D printing, an Ultimaker S2 + Connect (Ultimaker B.V., Utrecht, Netherlands) is used, while for FGF 3D printing, a PioCreat G5Pro (PioCreat, Shenzhen, China) is used. They are both equipped with a 0.8 mm ruby tip nozzle, which is suggested when dealing with fiber-reinforced materials. The material chosen to fabricate the specimens is Nylon Carbon, produced by FiberForce (Treviso, Italy), which is a short carbon fiber-reinforced PA12 (10% wt.). The choice of this material is motivated by the higher mechanical properties demonstrated by the addition of short carbon fibers to the polymeric matrix. The printing temperature is set to 230°C, and the bed temperature is kept at room temperature (25°C) to avoid unnecessary energy consumption, as hairspray is used to ensure the adhesion of the first layer. The printing speed is set to 50 mm/s, after verifying the printing quality, to shorten the cooling time of the layers and ensure improved adhesion [29,30].

To investigate the behavior of lattice structures at high strain rate, a cubic cellular infill is chosen, which has been previously investigated by the authors [31]. This structure is characterized by an array of closed cubic cells, with a vertically oriented diagonal. In this way, walls are made of a single pass of the nozzle, and the orientation of the cells ensures peak loads and unwanted buckling instabilities are limited. If cubic cells were in fact built with their walls parallel (and orthogonal) to the building direction (corresponding to the loading direction), high peak loads and high load drops would be observed [32,33]. The infill structure is available in the Cura slicing software, which optimizes its printing path, under the name of "cubic". Furthermore, cubic cells ensure theoretical air-tightening of the structure and help to avoid the inclusion of unwanted particles during operational life. Cylindrical specimens are built with a diameter of 40 mm and a height of 50 mm, varying the dimensions of the cells to obtain different overall densities of the components. To compare these structures to common engineering solutions, such as aluminum foams, densities of 200 g/l, 300 g/l, and 400 g/l were chosen, as shown in Fig. 1. Distances between the printed walls of the infill part are adjusted to obtain the desired specimens' weight. The external wall is built by a single line of material, so that its influence on the mechanical response of the components is limited, but it is still able to provide support for the printed lines of the infill part. This allows to focus the analysis on the infill structure, minimizing the load-bearing contribution of the external interface. A total of five specimens are printed for each configuration: two repetitions for quasi-static tests and three repetitions for high strain rate tests. Considering the six different specimens, the total number of specimens printed is 30.

As anticipated in the introduction section, the recycled material exhibits a higher density compared to the pristine one. This is likely due to both increased flowability [25,34] and different processing conditions of the FGF 3D printing technique [27], which is used for the recycled specimens. Pristine material processed by FFF 3D printing has been observed to introduce a high degree of porosity in the final 3D-printed specimens [27]. For this reason, different structures have to be designed to compare the same overall densities, and the results are clearly visible in Fig. 1: recycled specimens have larger cells compared to their pristine counterparts. Furthermore, recycled specimens show flow irregularities and few defects, as shown in Fig. 1. This is due to the difficulties of printing the recycled material in the form of shredded flakes, which introduces some complications in the feeding system and flow regularity.

2.2. Experimental setups

In this work, both quasi-static and high strain rate tests are conducted. Quasi-static tests are conducted using the electromechanical testing machine Zwick Z100 (ZwickRoell GmbH & Co. KG, Ulm, Denmark) with a 100 kN loadcell, at a speed of 0.5 mm/s to obtain an engineering strain rate of 0.1 s^{-1}. For these tests, a PixeLINK PL-B777 camera (PixeLINK, Ottawa, Canada) is used to record the collapse evolution of the structures, with a frame rate of 4 fps.

High-speed impact tests are conducted using a DIHPB apparatus, as

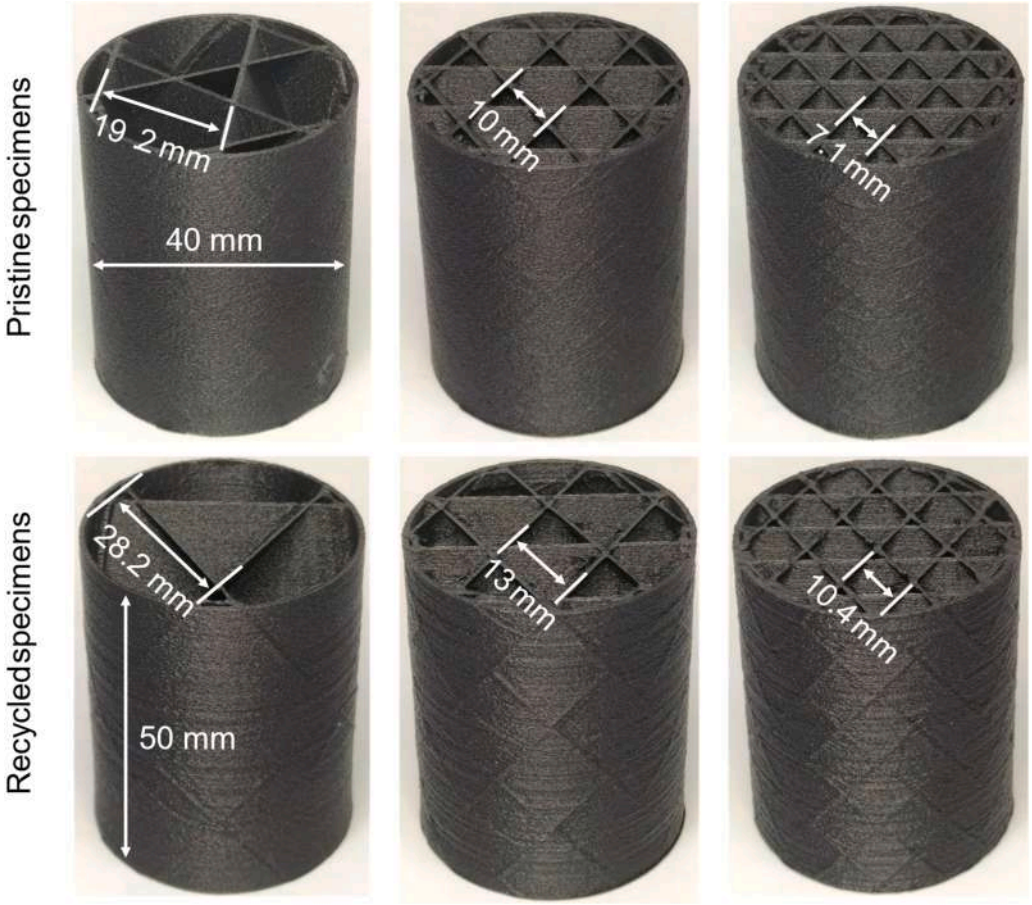

Fig. 1. 3D-printed pristine (top images) and recycled (bottom images) specimens. Dimensions of the infill structure, as well as the overall specimens' dimensions, are reported.

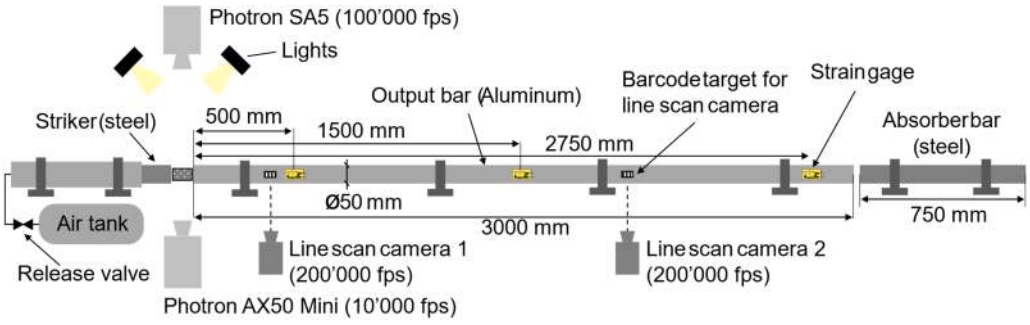

Fig. 2. DIHPB experimental setup scheme for high strain rate tests.

shown in Figs. 2 and 3. Steel strikers of different lengths (500 mm, 750 mm, and 1000 mm) are used to maintain the same impact speed when changing the specimens' densities. In this way, the impact energy is directly proportional to the specimen's density, ensuring an appropriate compression level at a comparable average strain-rate. In fact, higher specimens' densities require higher initial energy to produce comparable compression levels. Using different striker's length allows to increase the kinetic energy without changing the impact speed, increasing the impulse duration on higher densities specimens compared to shorter strikers. The 500 mm striker is used for 200 g/l specimens, and increasing lengths are used for specimens with increasing densities. Furthermore, the same initial engineering strain rate is obtained for all the specimens, independently of their density. The impact speed of the striker is set to 10 m/s, so that the initial engineering strain rate reaches 200 s^{-1}. An aluminum alloy (Al7082 T6) output bar with a length of 3000 mm is equipped with three KYOWA KSPB−1–350-E4 semiconductor strain gages (Kyowa Electronic Instruments Co., Ltd., Tokyo, Japan). All the bars and strikers have a diameter of 50 mm. Three strain gages are needed to allow for the wave deconvolution procedure needed to reconstruct the incident and reflected waves traveling inside the output bar. Due to the high deformation levels reached by the specimens, the transmitted wave is longer than the bar itself. This causes the wave to superimpose itself, which requires a deconvolution procedure to reconstruct the original wave at the specimen's interface with the bar. An absorber bar is placed at the free end of the output bar, so as to transfer energy and to provide a rigid stop if excessive displacement of the output bar is reached. Additionally, two line scan cameras Chromasens allPIXA neo 4k 10GigE (Chromasens GmbH, Konstanz,

Fig. 3. DIHPB experimental setup for high strain rate tests.

Germany) are pointed at barcode targets glued on the output bar, so that additional displacement measurements can be used to verify the correctness of the experimental data.The DIHPB requires the measurement of the striker's displacement to determine the axial displacement to which the specimen is subjected. Therefore, a Photron SA5 high-speed camera (Photron, San Diego, United States) is mounted above the setup to record the specimen's and striker's displacements. Additionally, a Photron AX50 Mini is used to record the tests at a lower frame rate, allowing for a higher resolution able to capture the whole specimen during its collapse. These videos are then used to compare the collapse behavior of the real specimens with their numerical counterparts. The setup is completed by an air tank connected to a controlled release valve, which is used to launch the striker. The recording system of both cameras and strain gages is triggered by the signal of a pair of photocells, which is mounted at the barrel end and activated by the striker's transit. The photocells are also used to automatically measure the impact speed of the striker. The proposed setup has been developed to allow a precise and compact experimental apparatus for the evaluation of large displacement tests on lattice structures. The present setup requires the precise positioning of the strain gages, as well as line scan cameras, which is fundamental for the deconvolution operations needed to derive the stress signal. Compared to a typical SHPB test, the strain measurements are derived on a single side of the experimental apparatus, and more equipment is needed to obtain satisfactory results.

2.3. Line scan cameras

Line scan cameras are used to measure the displacement of the bar in two different locations. Barcode-like adhesives are placed on the bar, and they are used for image tracking operations. Line scan cameras produce an image where every row of pixels (1×4096) represents an acquired frame. By analyzing the displacement of the recorded pattern in every row, one can evaluate the displacement and speed of the tracked target by appropriate dimensional calibration. Fig. 4 shows a typical image derived from a void test and the related speed of the bar, obtained by a MATLAB-implemented script. The measurement of displacements and speeds allows for both verifying the correctness of the strain gages' calibration and that of the wave separation procedure. The displacement measurements coming from the line scan cameras can be exploited in two different ways: using the derived speed measurement to calculate the stress inside the output bar, comparing it with the signals coming from the strain gages; using the displacement measurement to compare it with that reconstructed by the wave separation method, as will be shown in the following section.

Knowing the speed of the particle motion inside the wave and the material's mechanical impedance, one can calculate the stress acting on the bar by the following equation:

$$\sigma = v \cdot Z \tag{1}$$

Where Z is the mechanical impedance of the bar, calculated as:

$$Z = \rho \cdot C \tag{2}$$

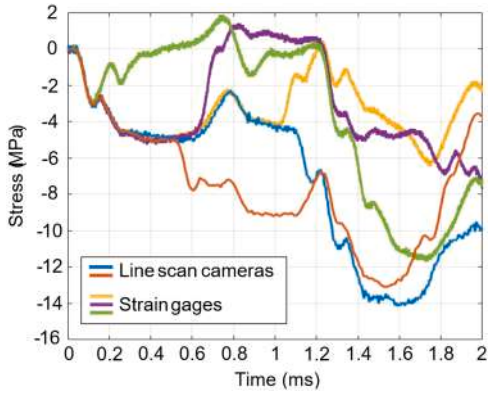

Fig. 5. Comparison between the stress calculated from the displacement measurements of the line scan cameras and the stress derived from the strain gage measurements. The signals are shifted in time, and the graph is zoomed to focus on the first few milliseconds of the test.

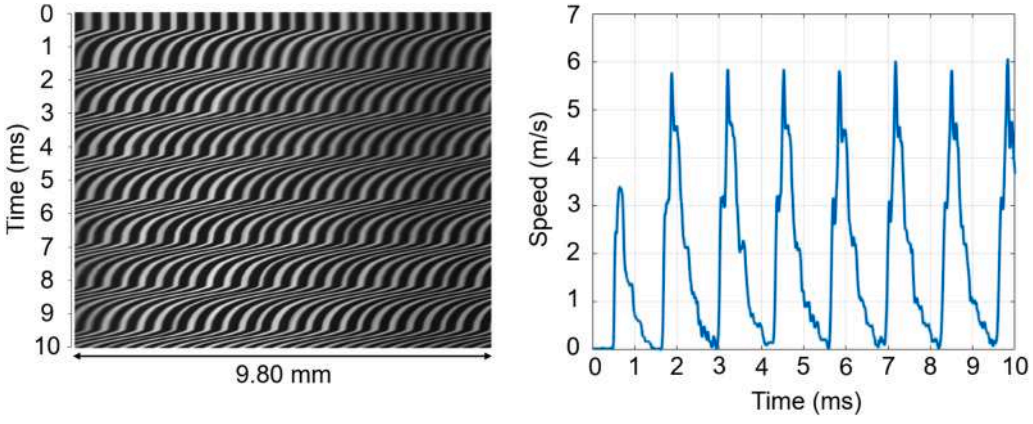

Fig. 4. Image generated by the linescan camera during an experiment (left) and output bar speed derived from the image analysis (right).

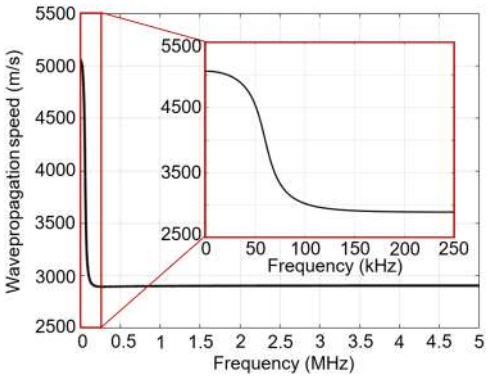

Fig. 6. Wave propagation speed inside an aluminum bar with a 50 mm diameter up to 5 MHz frequency. The zoomed detail shows the frequency range between 0 and 250 kHz, where the wave speed decreases to its steady value.

Where ρ is the material density, and C is the material's wave propagation speed. The comparison of the stresses derived from the strain gages and the line scan cameras, obtained in one of the experiments, is shown in Fig. 5.

The signals coming from the strain gages are in good agreement until the reflections of the wave arrive at the strain gages' locations. The last strain gage (green curve) experiences the reflection early, and its signal quickly deviates from the other two. The first two strain gages (yellow and purple curves) are in good agreement for a longer time since the reflection of the wave has to travel a longer distance. Strain gages and line scan cameras have overlapped signals until the reflection of the wave arrives at their different locations. From the line scan cameras' point of view, the reflection of the wave does not entail a decrease in the bar speed, but a further increase. As shown in Fig. 4, multiple reflections of the stress wave are registered by the line scan camera: the signal is clearly visible in the rapid change of the speed when the stress wave passes through the observation point. Since the stress signal derived from the line scan cameras comes from Eq. 1, it is clear to see that no variation in the sign of the stress is detected. Hence, the evaluation of the stress starting from the line scan signal cannot account for the stress decrease, as observed for the signal coming from the strain gages.

The good agreement between the line-scan-camera-derived and strain-gage-derived stress levels, before the reflection of the wave arrives, shows the correct dynamic calibration of the strain gages.

2.4. Wave separation procedure

As previously discussed, the large strain necessary to evaluate the mechanical behavior of the lattice structure entails the superimposition of the transmitted wave along the output bar. To analyze the mechanical performance of the specimens, it is hence necessary to adopt a wave separation on the signals coming from the strain gages. In this way, the loading wave can be accurately reconstructed, overcoming the need for a longer output bar [35–38]. Following the procedure described by Bussac et al. [39], the signals from the three strain gages are used to reconstruct the wave. The algorithm requires the knowledge of the bar's material properties, the knowledge of the dispersion function regarding the wave propagation speed, and the distance between the strain gages. If attenuation effects are observed (typical in polymeric bar setups), the deconvolution algorithm can be implemented by introducing the attenuation function. In the present work, an aluminum bar is used; hence, attenuation is considered negligible, and only dispersion effects are taken into account. Operating in the frequency domain, it is possible to reconstruct both the incident and reflected waves at a specific location of the output bar, thus obtaining the stress wave history. In this case, the stress wave history is reconstructed at the bar-specimen interface, so that the load acting on the specimen can be obtained. The dispersion law is derived from the solution of the Pochhammer-Chree equation for isotropic circular rods [40], and the result is shown in Fig. 6. The dispersion effect on the propagating waves inside a rod is due to the different wave propagation speed of each frequency component of the wave's spectrum. This produces a typical distortion effect, which changes the shape of the wave as it propagates along the bar. Higher frequency components propagate at higher speeds, while lower frequency components have lower propagation speed, as shown in Fig. 6. This entails the wave distortion effect, which is normally observed when a wave propagates along a medium. When a single strain gage is used, placing it sufficiently close to the specimen-bar interface would ensure that the dispersion effect can be neglected, whatever the length-to-radius ratio of the bar is. In this work, three strain gages are needed, and the wave must be observed as it travels along the bar. For this reason, the distortion effect due to dispersion must be taken into account.

As shown in Fig. 7, the strain gages' signals are used to reconstruct the incident and reflected waves in the output bar at the specified location. To verify the correctness of the wave separation procedure, the displacement obtained by the integration of the reconstructed strain is compared with the optical measurement of the line scan cameras.

As shown in Fig. 7, the wave separation technique is able to successfully reconstruct the incident and reflected waves, as demonstrated by the match of reconstructed and optical measurements of displacement. As reported by Bacon et al. [39], another way to verify the correctness of the wave separation procedure is to check the zero-stress condition at the free end of the bar. This condition is also satisfied, but it is not shown for the brevity of the discussion. Force equilibrium has

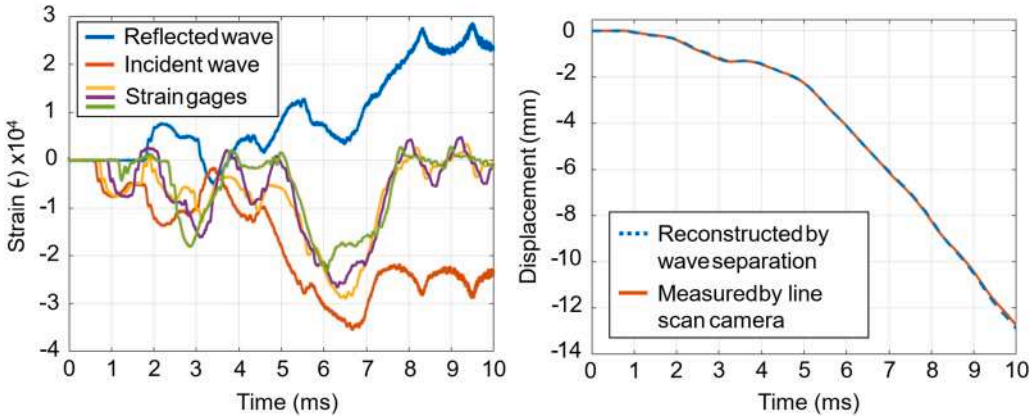

Fig. 7. Strain gages signals and reconstructed waves obtained by the deconvolution procedure at the specimen-bar interface (left). Comparison of the displacement reconstructed by wave separation at the line scan camera location, and obtained by the line scan camera (right).

already been shown to be reached for this type of structure in a past work by the authors [35]. In this past work, specimens of the same density and with the same speed were tested, ensuring force equilibrium with an SHPB test apparatus.

2.5. Crashworthiness indicators

In this section, the crashworthiness indicators that will be used in this work are presented. The indicators are chosen so that an accurate comparison with other works dealing with different technological solutions is possible. In this work, an engineering strain of 50% is chosen as the reference value for the crashworthiness properties of the specimens. This choice is motivated by the observation of the experimental curves, as the onset of densification can be associated with this level of engineering strain. Other works on the crashworthiness of thin-walled structures propose the definition of the effective deformation as a non-arbitrary deformation value as a reference for energy absorption properties [41–43]. However, due to the particular behavior of the lattice structures presented in this work, the use of the effective deformation entails highly variable crashworthiness indicator values, which are not representative of the behavior of the specimens. For example, a sudden drop of load close to the densification stage leads to the maximum energy absorption efficiency, while the structure still has energy absorption potential left before densification. Thus, the choice of a common deformation level is more appropriate to evaluate the energy absorption characteristics of the lattices, here called $d_{0.5}$, which corresponds to an engineering strain level of 0.5. The mean crushing force (MCF), corresponding to the force level of an equivalent ideal energy absorber, is calculated as:

$$MCF = \frac{\int_0^{d_{0.5}} F(s) \quad ds}{d_{0.5}} \tag{4}$$

The specific energy absorbed (SEA) is a powerful indicator of the crashworthiness of the structures, which normalizes the total energy absorbed (until reaching $d_{0.5}$) by the mass contributing to the absorption. SEA values should always be reported with the corresponding density of the structures, since higher densities inevitably entail higher SEA values. Hence, the comparison should be conducted with similar values of density. The equation used to calculate SEA is the following:

$$SEA = \frac{\int_0^{d_{0.5}} F(s) \quad ds}{m} \tag{5}$$

The last crashworthiness indicator used in the present study is the crushing force efficiency (CFE), which is a measure of the maximum deceleration experienced, compared to the mean deceleration during the energy absorption stage. This parameter is particularly useful when evaluating the safety of goods and people in the design stage of energy absorbers. The CFE is calculated as follows:

$$CFE = \frac{MCF}{IPF} \tag{6}$$

Where IPF is the initial peak force usually experienced at the end of the elastic or pseudo-elastic deformation stage, before the initial buckling of the structure. A value of CFE close to 1 indicates that the examined structure behaves similarly to an ideal energy absorber.

3. Experimental results

3.1. Quasi-static tests

Quasi-static tests are conducted to compare the quasi-static behavior with the high strain rate one, observing differences in both the load levels and collapse modes. The tests are conducted with an electromechanical universal testing machine at a loading speed of 0.5 mm/s. Two

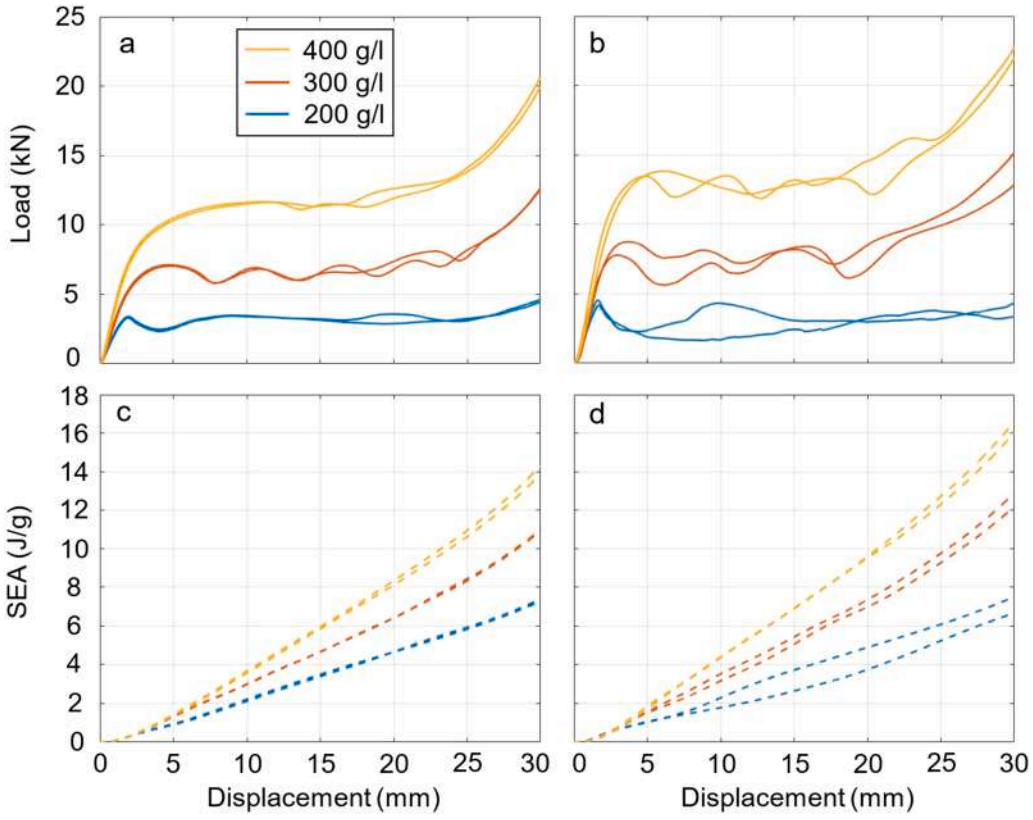

Fig. 8. Load-displacement and specific energy-displacement curves of the quasi-static tests. Images on the left are related to pristine specimens (a,c), while images on the right are related to recycled specimens (b,d).

repetitions for each specimen type are obtained to verify the repeatability of the experimental results. The load-displacement and energy-displacement curves of the first phase of testing are shown in Fig. 8.

The quasi-static behavior of 3D-printed pristine and recycled specimens, both in terms of load-bearing and energy-absorbing capabilities, is comparable. Both types show an expected increase in mechanical properties with the increase in the specimen's density. Observing the same densities across pristine and recycled specimens, it is possible to observe a very similar collapse behavior of the structures: apart from pristine 400 g/l specimens, a peak load is reached, and a following plateau-like region is observed, with limited load oscillations. The load oscillations are associated with the buckling and collapse of subsequent arrays of cubic cells, which are usually crushed in unison on the same horizontal plane. This is particularly evident for the 300 g/l specimens, where the number of cells is high enough to prevent an evident load drop, as in the 200 g/l specimens, and low enough to not exhibit a foam-like behavior in the plateau region, as in the pristine 400 g/l.

Relevant differences are, however, observed between pristine and recycled specimens: experimental results show a clear distinction between the repeatability of the tests. Pristine specimens, produced by filament in a more controlled production process, exhibit almost identical behavior between the two repetitions. Recycled specimens, characterized by a more difficult production process [27], exhibit a degree of difference between the two repetitions. The printing process of recycled material poses more challenges, and material flow instabilities lead to defects during the production of large components [44,45]. The distance between the experimental curves is gradually reduced as the density of the specimen is increased, showing that defects of the production process are mitigated in denser structures. Looking at Table 1, where energy-absorbing properties are listed, a clear trend is observable in the dispersion of results of the recycled specimens: the higher the density, the lower the dispersion of results.

Interestingly, recycled specimens exhibit higher mechanical properties and energy-absorbing capabilities. While 200 g/l recycled specimens are affected by their very thin structure (Figs. 1 and 9), and thus show comparable or lower SEA, 300 g/l and 400 g/l recycled specimens exceed the energy-absorption capability of pristine specimens.

Fig. 9 shows the specimens after the compression tests. Collapse modes are driven by the internal infill structure, with layer-wise collapse of cubic cells, for both recycled and pristine materials. However, the collapse modes are different between recycled and pristine materials: the first show localized collapse behaviors, probably reflecting possible printing defects and asymmetries; the second show more homogeneous collapse modes, which are more evident for higher densities. For recycled specimens, the collapse of a single row of cells can be observed, while pristine specimens show a distributed buckling of the cell walls across different heights of the specimen. The ordered geometry of the infill structure drives a symmetrical collapse mode in 300 g/l and 400 g/l specimens (more pronounced in pristine specimens). For 200 g/l specimens, the density of the structure is not sufficient to guarantee an ordered collapse mode; thus, their mechanical response is less stable and prone to greater load oscillations.

Recycled specimens experience fracturing of printed walls: both intra-layer and inter-layer fractures are observed, especially in 200 g/l and 400 g/l recycled specimens, respectively. This is due to the longer free lengths and lower densities of 200 g/l, which results in walls bending freely and breaking along the weakest material's direction (vertical printing direction) (Fig. 9d). Conversely, 400 g/l specimens have shorter free lengths; thus, printed walls experience radial stretching, which drives failure mechanisms starting from jointure points of different walls, as observable in Fig. 9f. Regarding the 300 g/l recycled specimens, the density provides sufficient stress redistribution across different walls, but does not entail excessive radial stretching of the walls; thus, no failure is observed (Fig. 9e). Fracturing of recycled specimens is explained by the reduced strain at failure of the recycled printed material, already observed in a previous work by the author [27].

Pristine specimens do not show any sign of failure, although they experience analogous strain levels during the compression tests. They show a greater ability to withstand bending and high deformation of the printed walls (Figs. 9a, 9b, and 9c). Furthermore, since no fracturing occurs, load oscillations are appropriately attributed to the walls' buckling and are less pronounced compared to the recycled specimens.

The reason for the differences observed in these tests is attributed to the differences introduced by the printing process. In a recent work, the authors studied the recycling and printing process of the same short-fiber-reinforced material, highlighting three major aspects: the first being the comparable mechanical properties of the recycled material and the pristine one (using FGF printing); the second being the higher mechanical properties obtained by FGF printing compared to FFF printing; the third being the increased density of the material produced by FGF printing, compared to the relatively high porosity observed in the FFF counterpart [27]. In this case, recycled specimens benefit from higher mechanical properties due to FGF printing, which fundamentally reduces the material's porosity. At the same time, they are affected by the thinner geometry, which is required to obtain the same weight as their pristine counterparts. These two opposed mechanisms produce different effects based on the 3D-printed structure's density: lower densities (200 g/l) suffer from excessive structure thinning, while higher densities exhibit more stable structures, thus benefiting from the increased mechanical properties.

Table 1 sums up the results of the quasi-static compression test. The SEA of 300 g/l and 400 g/l recycled specimens is 13.4% and 16% higher compared to their pristine counterparts, respectively. Conversely, the SEA of the 200 g/l recycled specimens is 3.7% lower than that of their pristine counterparts. Although having higher energy absorption, 300 g/l and 400 g/l recycled specimens have slightly lower crush force efficiency values, while 200 g/l recycled specimens exhibit a noticeably lower crush force efficiency value. The reason for the latter observation still comes from the very thin structure of the 200 g/l recycled specimens, which entails a noticeable load drop after the first buckling of the walls. As indicated by the coefficients of variations presented in Table 1, pristine specimens show more repeatable results, while higher dispersion is observed for recycled specimens. Furthermore, more dispersed results are observed for lower densities compared to higher densities, showing that a denser structure mitigates localized effects more efficiently. Overall, the dispersion of the results is limited, especially for pristine specimens, and the coefficients of variation only exceed 10% in the case of the recycled 200 g/l specimens, which is more affected by printing defects.

Compared to typical engineering solutions as aluminum foams, higher specific energy absorption values are reached. Cheng et al. [46] investigated the energy absorption properties of aluminum foams in quasi-static compression tests, obtaining SEA values of 4.31–4.98 J/g for foam densities of 360–460 g/l. Wang et al. [47] conducted compression tests on aluminum foams in the range of 217–414 g/l, observing values of SEA between 3.75 J/g and 6.05 J/g, respectively. This shows how

Table 1
Energy-absorption parameters of the quasi-statically tested 3D-printed structures. Coefficients of variation are reported in brackets.

Pristine	**200 g/l**	**300 g/l**	**400 g/l**
Peak load	3353 N (2.4%)	7077 N (0.9%)	11650 N (0.3%)
Mean load	3085 N (1.4%)	6781 N (1.4%)	12179 N (0.6%)
CFE	93% (3.8%)	96% (0.0%)	105% (0.7%)
SEA	5.88 J/g (1.2%)	8.38 J/g (0.8%)	10.79 J/g (2.1%)
Recycled	**200 g/l**	**300 g/l**	**400 g/l**
Peak load	4374 N (5.6%)	8266 N (8.2%)	13654 N (1.9%)
Mean load	2934 N (16.5%)	7857 N (8.0%)	13410 N (1.8%)
CFE	67% (10.5%)	95% (0.0%)	99% (3.6%)
SEA	5.66 J/g (10.5%)	9.50 J/g (3.7%)	12.52 J/g (2.4%)

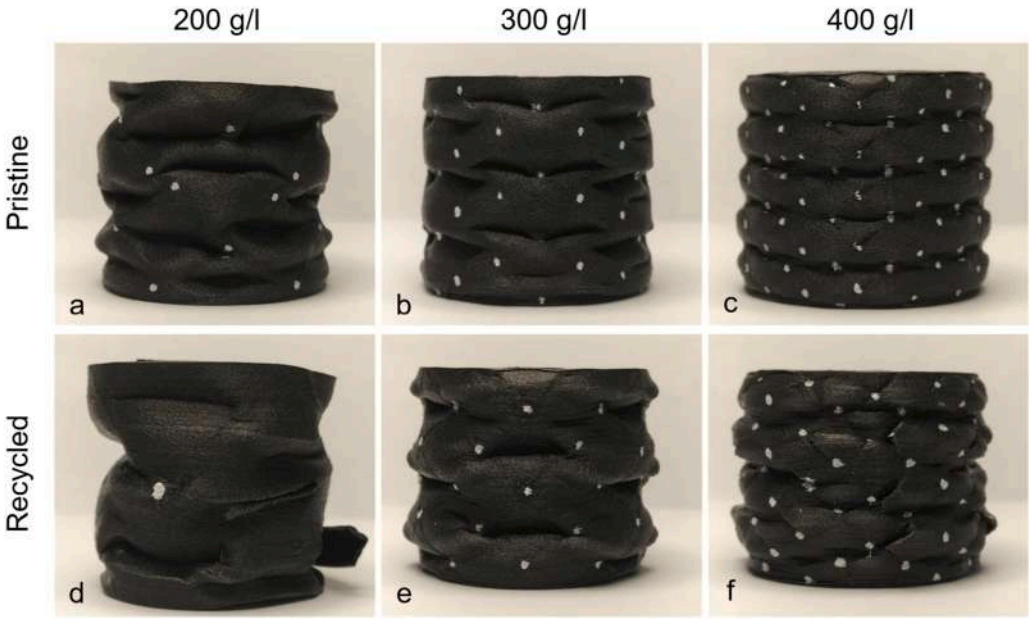

Fig. 9. Collapsed specimens after the quasi-static compression tests.

3D-printed polymeric lattice structures can be a valid substitute for common solutions as aluminum foams. Values of SEA found in the present work are comparable with other studies on the mechanical properties of 3D-printed polymeric lattice structures investigating similar densities. As an example, Yu et al. [48] investigated the quasi-static performance of PLA Kelvin lattices with densities in the range of 220–360 g/l, observing SEA values ranging from 8 J/g to 11.5 J/g. Feng et al. [11] studied the quasi-static compression properties of two types of TPMS 3D-printed structures in a density range of 240–480 g/l. They reported SEA values between 5.8 and 9.2 J/g for the "Diamond" lattice structure, while values between 5.7 and 7.7 J/g were obtained for the "Gyroid" structure.

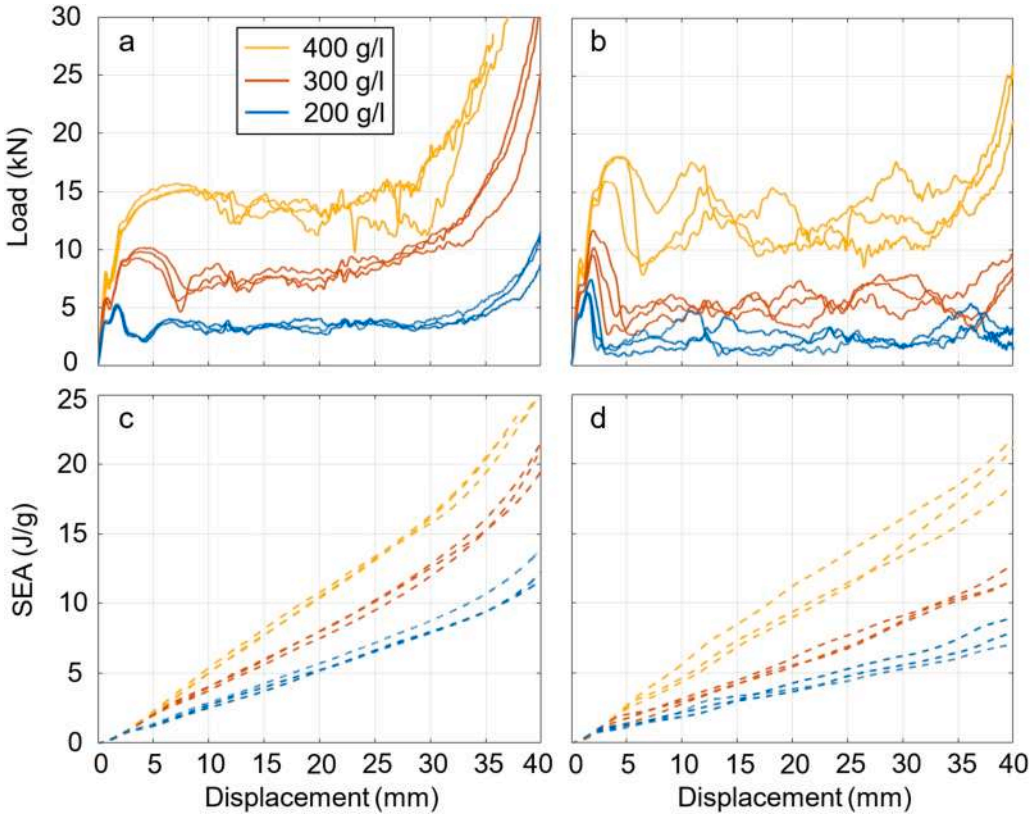

Fig. 10. Load-displacement and specific energy-displacement curves of the high strain rate tests. Images on the left are related to pristine specimens (a,c), while images on the right are related to recycled specimens (b,d).

Compared to auxetic or truss lattice structures, the ones tested in this work exhibit higher mechanical properties and higher energy absorption capability. As an example, Quan et al. [49] tested the quasi-static response of auxetic continuous fiber-reinforced 3D-printed structures, observing SEA values of 1.34–1.75 J/g depending on the tested direction. Sun et al. [50] investigated the energy absorption behavior of polymeric 3D-printed truss lattices, obtaining values of SEA of 2.5 J/g for a specimen's density of 180 g/l. Ozturk et al. [51] investigated the compression properties of different lattice structures in the density range of 314–425 g/l, obtaining SEA values of 1.19–2.43 J/g.

3.2. High strain rate tests

High strain rate tests are conducted to test the specimens in real operating conditions, aiming for their application as crash-absorbing structures. Three equal specimens are tested for each experimental configuration. Many studies investigate the energy-absorbing properties of lattice structures just by conducting quasi-static tests [52]. However, the strain rate dependency of short-fiber-reinforced polymeric material has already been documented [53,54]. Past studies have shown that a good quasi-static mechanical performance does not necessarily entail a good high strain rate mechanical behavior [5,35]. This aspect is fundamental when dealing with the design of such components, and high-speed impact testing is thus necessary to assess the evaluation of their real impact mitigation capability.

In this work, 3D-printed short-fiber-reinforced polymeric structures are tested by a DIHPB apparatus, equipped with two high-speed cameras and two line scan cameras. This apparatus guarantees the most accurate load and displacement measurement, overcoming measurement problems commonly observed in drop weight impact tests, such as load cell ringing and indirect measurements. Especially, load cell ringing is a common obstacle to an accurate load evaluation, since it produces numerous fictitious oscillations in the final experimental results [55]. The use of strain gages with a wave separation technique, combined with the high-speed optical measurement of the striker's displacement, ensures the high-quality evaluation of the mechanical properties of the analyzed structures.

The results of the second phase of testing are shown in Fig. 10. The mechanical behavior of the 3D-printed specimens is strongly influenced by strain rate. High strain rate curves of load and specific energy absorbed clearly show a strain rate dependency of the printed material when compared with the curves of the quasi-static tests. The effects of the strain rate on the tested specimens are both positive and negative in terms of mechanical performance, depending on the material and on the structure's density. Table 2 reports the energy absorption parameters of the specimens tested in high strain rate conditions.

Starting from pristine specimens, the effect of the loading rate on the load-bearing and energy-absorbing capability of the 3D-printed structures is definitely beneficial. Independent of the density, an increase in the peak loads, mean loads in the plateau region, and specific energy absorption is observed. In terms of SEA values, pristine specimens tested at high strain rate exhibit an increase of 15%, 19% and 22% for 200 g/l, 300 g/l, and 400 g/l densities, respectively. The crush force efficiency experiences a reduction based on the density of the specimens, as the lower the density, the higher the decrease in crush force efficiency. This is because the mean loads do not increase as much as the peak loads, due to fracturing of the printed walls. As already observed in other works on polymers, the increase in strain rate leads to an increase in ultimate stress, but reduces the maximum strain at break [56,57]. Although extensive fracturing of the specimens occurs, the load-displacement is only partially affected, with a major effect on lower densities, as expected. The fracturing behavior entails a delayed densification behavior since the material is free to expand outward. As observed for the quasi-static tests, the results of the strain rate tests on pristine specimens are repeatable, and only one of the 400 g/l specimens deviates from the average behavior, close to its densification stage.

Regarding the recycled 3D-printed specimens, the strain rate entails a clearly negative effect on the mechanical performance of the structures. The fracturing behavior already experienced in the quasi-static tests is further exacerbated, thus leading to substantial load drops and instability. Unlike pristine specimens, the load-bearing and energy-absorbing capabilities of the recycled specimens are worsened by the effect of the strain rate. Although the ultimate tensile test is probably increased by the increase of strain rate, the further reduction of the ultimate strain at break prevents the specimens from absorbing energy by plastic deformation. The SEA values decrease by 15%, 25%, and 4% for densities of 200 g/l, 300 g/l, and 400 g/l, respectively. Concerning the CFE, notable decreases are observed compared of the quasi-static values, thus confirming that despite a peak load increase, the load borne by the structures is lower. This has to do with the extended fracturing behavior, which is exacerbated by the high strain rate testing conditions. As observed by the frames of the video recordings shown in Fig. 11, the material behaves in an evidently brittle way, substantially deviating from its quasi-static behavior. Among the recycled specimens, 300 g/l ones are the most affected by the strain rate. This is likely due to the inner structure of the 300 g/l specimen: while in quasi-static conditions, it avoided fracturing due to a good balance of distributed stress and freer expansion, as the collapse behavior changed due to strain rate, it worsened the load-bearing capacity. Structures with 200 g/l density have longer free lengths, which avoid excessive embrittlement, providing sufficient space for the walls to adapt to the rapid deformation (Fig. 11). Structures with 400 g/l density have a denser structure, which is subjected to extensive fracturing and debris ejection (Fig. 11). However, smaller free lengths (smaller cells) allow for a more gradual load drop as the fracture advances along the axial direction, resulting in a smoother behavior. Unlike the matrix pristine material, the recycled one is characterized by a higher density. In the event of high-speed impacts, a certain degree of porosity can be beneficial to mitigate local stress peaks due to impulsive loads, providing dissipation [58–61]. The attenuation behavior of porous materials can guarantee a higher deformation capability of the base material, exploiting the voids as a means of deformation compensation. When the printed walls are subjected to extensive bending (due to buckling), the presence of voids can help the material to withstand higher deformations without breaking [62,63]. The pores included in the printed material can, in fact, act as a "free" deformation mechanism, with limited material involvement and stress generation. In this way, the FFF printed material can better bear the embrittlement entailed by the effect of the strain rate increase.

To further investigate this matter, micro-CT scans of the materials printed with the same printing parameters are analyzed to derive the porosity level and deepen the understanding of the materials' microstructure. Micro-CT scans are derived from a previous work by the authors where the same material was printed using the same printing parameters by FFF and FGF printing [27]. A MATLAB code is developed to assess the porosity levels inside pristine and recycled materials. The results of the analysis show a mean porosity value of 16% for the pristine

Table 2
Energy-absorption parameters of the high strain rate tested 3D-printed structures. Coefficients of variation are reported in brackets.

Pristine	**200 g/l**	**300 g/l**	**400 g/l**
Peak load	5549 N (2.5%)	9800 N (4.6%)	15369 N (2.1%)
Mean load	3383 N (1.3%)	7725 N (4.6%)	13726 N (2.0%)
CFE	62% (3.8%)	79% (1.6%)	89% (4.0%)
SEA	6.78 J/g (4.9%)	9.94 J/g (3.9%)	13.21 J/g (1.0%)
Recycled	**200 g/l**	**300 g/l**	**400 g/l**
Peak load	6746 N (9.7%)	10537 N (10.4%)	17368 N (6.9%)
Mean load	2217 N (8.2%)	5160 N (7.2%)	12247 N (12.8%)
CFE	33% (2.3%)	49% (10.3%)	70% (9.8%)
SEA	4.82 J/g (9.0%)	7.10 J/g (7.0%)	12.06 J/g (11.0%)

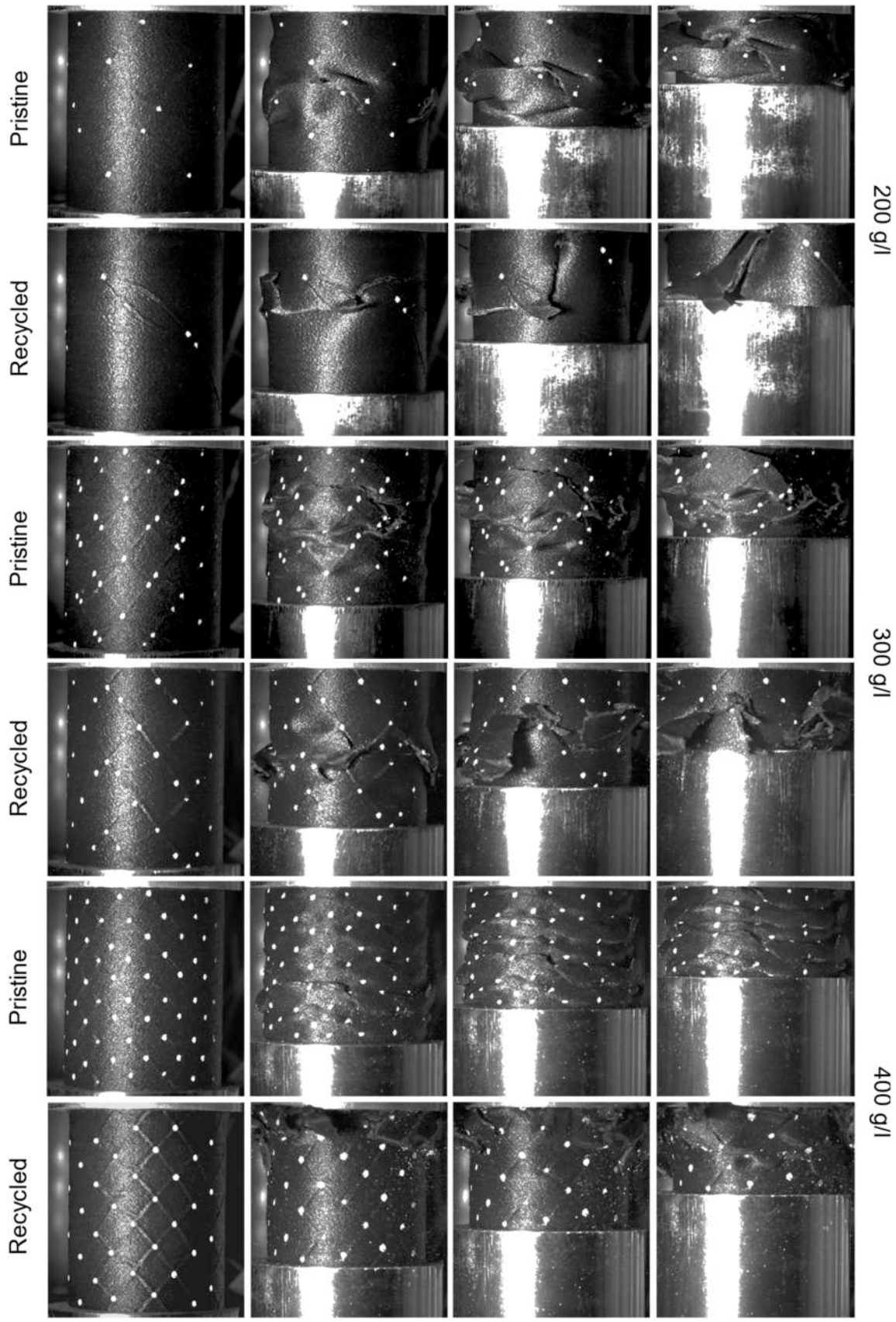

Fig. 11. Video frames of the high-speed impact tests.

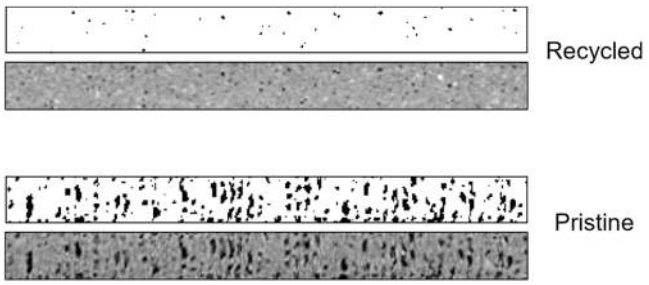

Fig. 12. 2D slices of recycled and pristine material with enhanced contrast to highlight pores (black) and material (white).

FFF-printed material, while only 0.6% for the recycled FGF-printed material. Fig. 12 shows a pair of reconstructed 2D slices used for the porosity evaluation.

The major difference in porosity observed between the pristine and recycled materials reveals an intrinsic difference in the printing process, confirming the hypothesis of a major impact of porosity on the mechanical performances of the lattice structures.

Despite the reduced energy-absorption performance, recycled specimens maintain satisfactory SEA values. Compared to quasi-static tests, the same considerations about dispersion of the results hold for dynamic tests. The dispersion coefficients are slightly higher compared to the quasi-static testing, especially for recycled specimens. Only 300 and 400 g/l specimens show some values higher than 10%, meaning that a sufficient repeatability has been reached. Analyzing the results of common engineering solutions for energy-absorbing structures, steel and aluminum tubes usually show SEA values of about 10–13 J/g, with lower costs compared to pristine FFF material [64]. However, the cost of the recycled material is practically zero (as 1 kg of material is estimated to cost around 0.10 € when printed). CFRP tubes represent the highest performance components for energy-absorbing purposes, with SEA values up to 60 J/g, while their cost is incomparably higher [64]. Compared to other works dealing with the high strain rate behavior of 3D-printed polymeric lattice structures, similar results are obtained. Song et al. [65] investigated the dynamic behavior of hybrid TPMS structures printed with PLA, observing relevant differences between the quasi-static and dynamic regimes. They obtained values of 13.7–15 J/g for structures with an overall density of 400 g/l when tested laterally or axially to the printed direction, respectively, at an engineering strain of 50%. Feng et al. [11] studied the dynamic compression properties of two types of TPMS structures in a density range of 240–480 g/l, resulting in values ranging from 6.8 J/g to 11.2 J/g. As a result, the dynamic energy absorption capability was found to be improved by the increased strain rate. Bouteldja et al. [5] tested 3D-printed ABS and tough PLA cylindrical bulk specimens in quasi-static and high strain rate conditions. They observed that yield stress and ultimate stress more than doubled for some printing configurations, maintaining a relatively ductile behavior when increasing the strain rate. In the same work, the authors tested some truss lattices and observed decreases in energy absorption for all the lattice structures and materials used. This further confirms that the sole study of the strain rate dependency of the base material is not sufficient to estimate the mechanical performance of 3D-printed lattice structures.

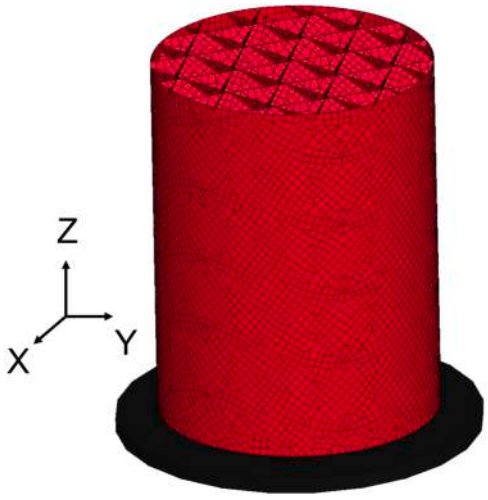

Fig. 13. Finite element model of the pristine 400 g/l specimen.

Table 3
Elastic and yield properties of the anisotropic material model.

Pristine	ρ (g/cm^3)	E_{zz} (MPa)	E_{xx} (MPa)	E_{yy} (MPa)	G_{xz} (MPa)	G_{xy} (MPa)	G_{yz} (MPa)
	0.8	680	1950	1950	350	450	350
	ν_{xz} (-)	ν_{xy} (-)	ν_{yz} (-)	σ_{zz} (MPa)	σ_{xx} (MPa)	σ_{yy} (MPa)	σ_{xz} (MPa)
	0.16	0.3	0.16	39	52	52	27
Recycled	ρ (g/cm^3)	E_{zz} (MPa)	E_{xx} (MPa)	E_{yy} (MPa)	G_{xz} (MPa)	G_{xy} (MPa)	G_{yz} (MPa)
	0.9	1100	2400	2400	400	500	400
	ν_{xz} (-)	ν_{xy} (-)	ν_{yz} (-)	σ_{zz} (MPa)	σ_{xx} (MPa)	σ_{yy} (MPa)	σ_{xz} (MPa)
	0.2	0.3	0.2	45	60	60	32

4. Finite element analysis

4.1. Finite element model definition

In this section, the finite element model developed to simulate the mechanical behavior of the 3D-printed lattice structures in dynamic conditions is presented. The software used for the calculations is LS-DYNA, which is particularly indicated for explicit simulations of crash scenarios.

Each structure is modelled and simulated using its complete geometry, and two different material models are employed to model the behavior of pristine and recycled materials, respectively. A mesh with fully integrated shell elements with an average dimension of 1 mm is used. Fig. 13 shows an example of a structure (pristine 400 g/l specimen) modeled in the LS-Prepost pre- and post-processing software:

The material model used for the 3D-printed material is an anisotropic material model with Hill's yield criterion and an isotropic hardening law (MAT_ANISOTROPIC_ELASTIC_PLASTIC). This material model is chosen to represent the strong anisotropy that characterizes the fiber-reinforced 3D-printed material, as already observed in previous works by the authors [66,67]. These works discuss the material modeling in detail, which will not be repeated herein. The anisotropy of the material is treated so that the x and y directions (horizontal directions) have the same mechanical properties, while the vertical direction has lower mechanical properties. Hence, the material is modeled as a transversally isotropic material. Hill's anisotropic yield criterion is shown in Eq. 7:

Table 4
Erosion properties of the material. Three different values are reported for EFFEPS (maximum equivalent strain at failure) for 200 g/l, 300 g/l, and 400 g/l specimens, respectively.

Pristine	SIGP1 (MPa)	EFFEPS (-)
	70	0.5–1.2–1.2
Recycled	SIGP1 (MPa)	EFFEPS (-)
	80	0.3–0.3–0.5

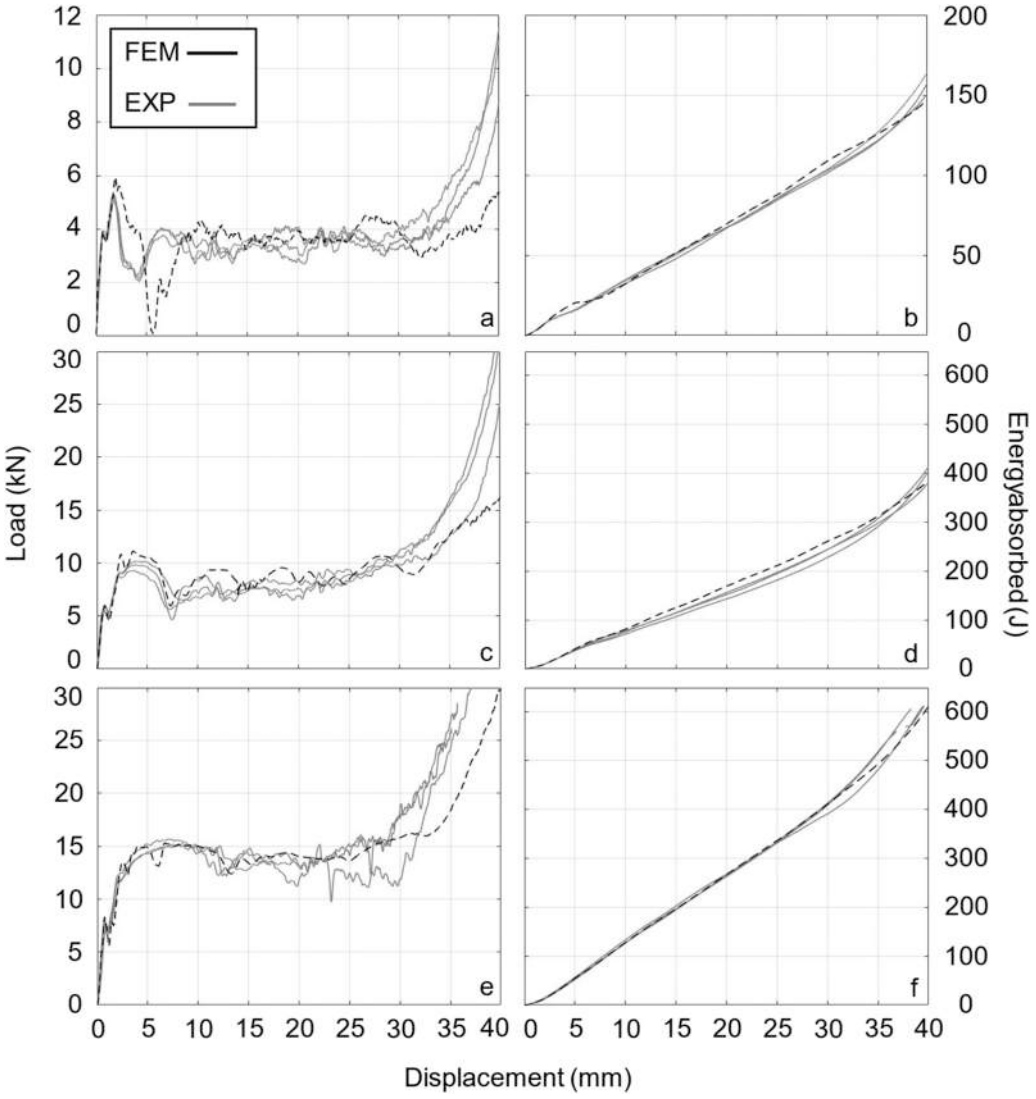

Fig. 14. Comparison of the experimental and numerical curves of the pristine specimens in high strain rate conditions.

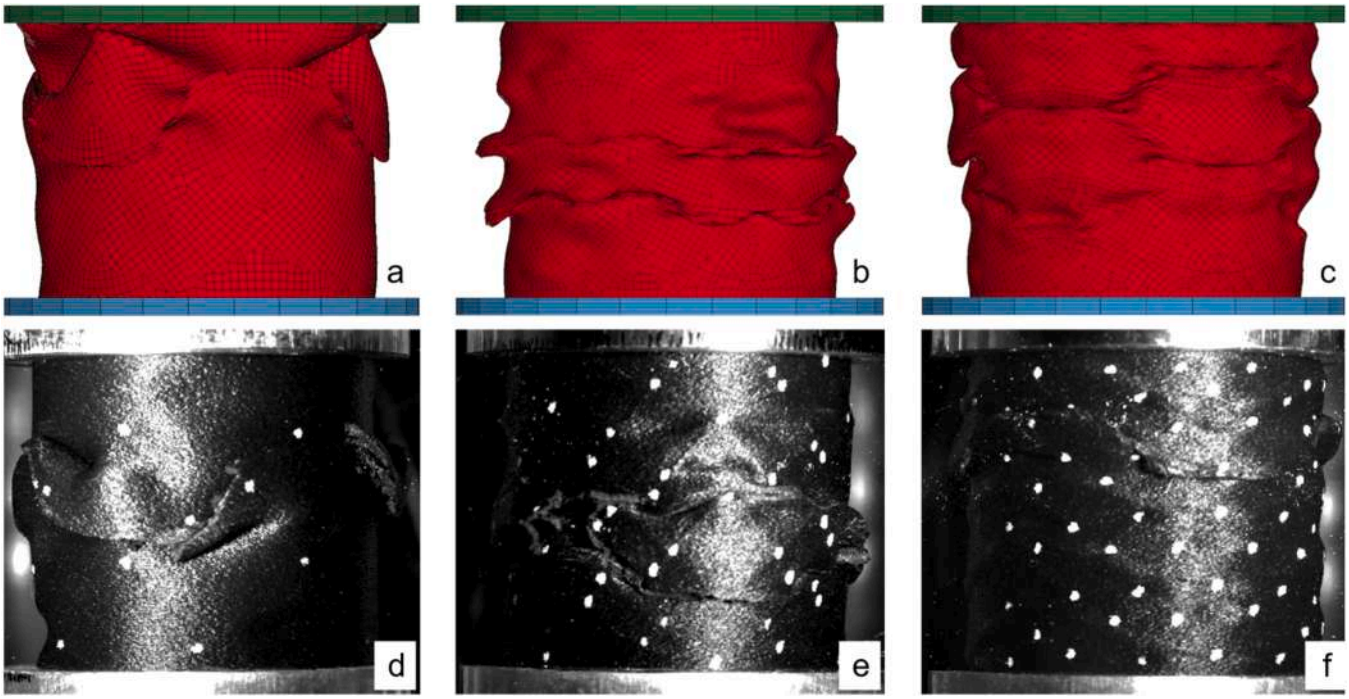

Fig. 15. Collapse behavior comparison between experimental tests and numerical simulations of pristine specimens.

$$F(\sigma_{xx}-\sigma_{yy})^2+G(\sigma_{yy}-\sigma_{zz})^2+H(\sigma_{zz}-\sigma_{xx})^2+2L\tau_{xy}^2+2M\tau_{yz}^2+2N\tau_{xz}^2=1 \quad (7)$$

Coefficients F, G, H, L, M, and N are automatically calculated by the finite element software starting from the yield values presented in Table 3. For a detailed explanation of the material modeling, the reader is invited to refer to a previous work by the authors [66].

Table 3 shows the mechanical properties used in the simulations. Some attempts were made using an isotropic material model, but it failed to accurately represent the mechanical behavior of both materials in the different density configurations. Especially for the 200 g/l specimens, the isotropic material model fails to represent the collapse behavior, as the hypothesis of isotropy relies on a sufficient number of cells across the structure [35]. MAT_ADD_EROSION is used to model the failure behavior of the 3D-printed material. The failure criterion is chosen by combining the maximum principal stress and the maximum equivalent strain so that both conditions must be achieved to entail material deletion. The erosion option permanently deletes elements, so the densification behavior is hard to mimic. Higher densities are especially prone to excessive failure compared to the experimental results, and the deletion of elements entails the impossibility of simulating their densification stage. For this reason, the maximum equivalent strain allowed is increased as the density of the specimen increases, as shown in Table 4. This modeling strategy limits the predictive value of the finite element model, while still providing a simple and fast way of tuning just one parameter to represents the failure behavior of the structures. Two rigid walls are modeled to impose the deformation on the specimens at a speed of 10 m/s.

The material properties are modified starting from quasi-static tests conducted in previous work by the authors on the same fiber-reinforced material, both in pristine and recycled forms [27,67]. The material model is not able to represent the difference between tensile and compressive properties, so unique numbers must be used. Hence, a combination of tensile and compressive properties is chosen to obtain the best fit. Furthermore, since no high strain rate properties are available, the values chosen reflect an increase compared to the quasi-static properties evaluated by tensile and compression tests. Lastly, the strain hardening law is chosen as a linear increment of 40 MPa over an equivalent plastic strain deformation of 0.5, for both materials. This is a simplification coming from the experimental observation of previous tests, including an increase due to strain rate effects. Using the same values for both materials comes from the hypothesis that the same plastic evolution for both recycled and pristine printed polymers occurs. The maximum principal stress at failure is chosen based on the tensile values reported in previous works by the authors, addressing the increase due to the strain rate effect. The maximum equivalent strain is not simply calculated due to the anisotropic nature of the material [68]. Moreover, as previously discussed, the erosion of elements requires the variation of the strain at break to correctly model the densification behavior and to avoid excessive failure. Hence, the parameter (EFFEPS) is fitted based on the comparison between experimental and numerical results.

4.2. Comparison between experimental and numerical results

Figs. 14 and 15 show the comparison between the experimental and numerical results for the pristine specimens, both in terms of load-displacement and energy-displacement curves, and in terms of collapse behavior. The models accurately represent the load-displacement and energy-displacement curves of their experimental counterparts, with a maximum average error in the energy absorption estimation of 7.3% for the pristine 300 g/l specimen (Fig. 14c). Specifically, the first peak and the late densification stage are more prone to showing some delays between experimental and numerical curves. In terms of load, this effect leads to higher errors while comparing loads at the same displacement, as can be seen for the 200 g/l pristine specimen (Fig. 14a). However, in terms of energy absorption curves, these errors are mitigated and do not influence the results substantially (Fig. 14b). The finite element models are able to reproduce the main features of the specimens' behavior correctly: initial peak loads, mean force during the deformation stage, and densification onset (with some delay due to the erosion criterion effect). The initial pseudo-elastic stage of the compression test is particularly well represented, with a perfect match between the slope of the experimental and numerical curves, proving that the elastic matrix is finely tuned. Notably, the first buckling instability, represented by the small load peaks at the beginning of the curves,

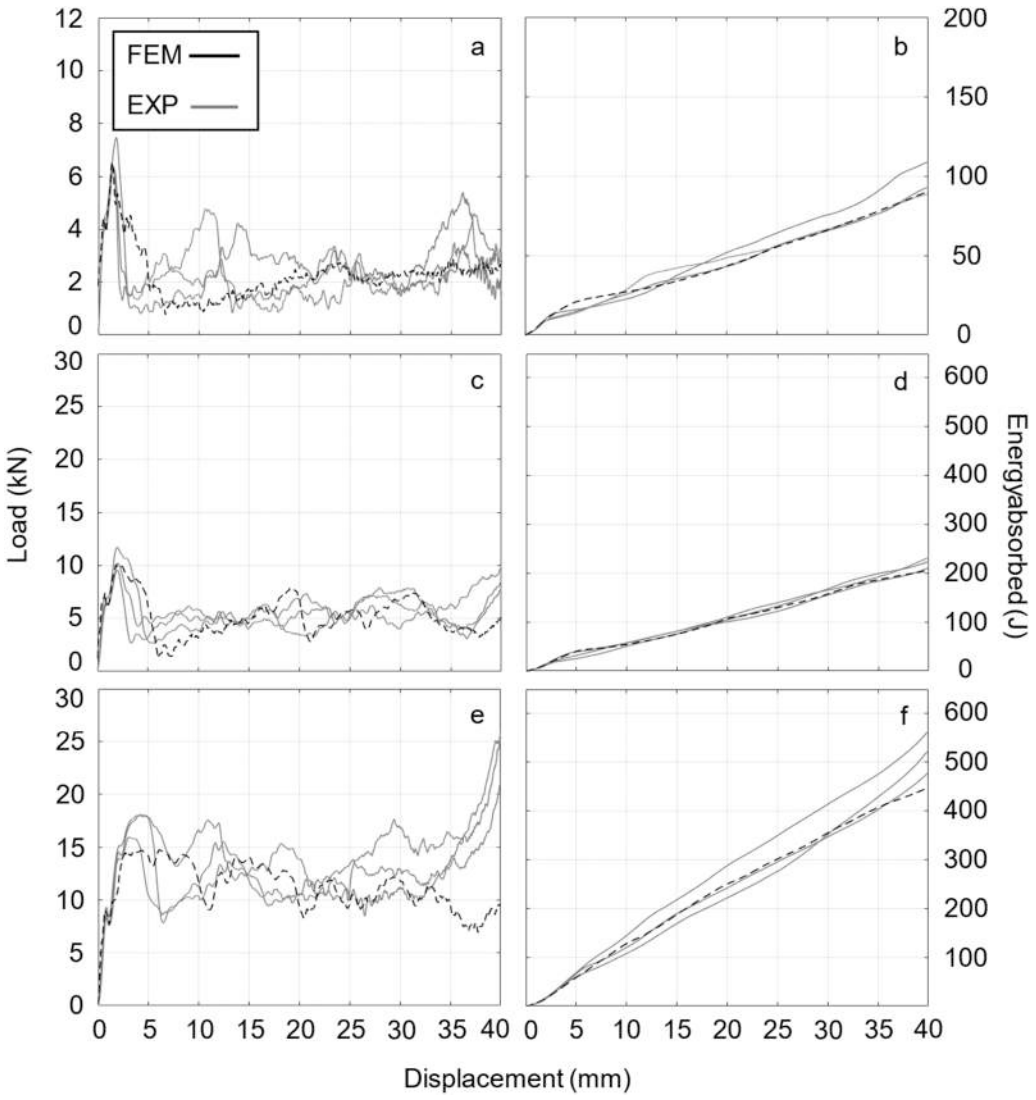

Fig. 16. Comparison of the experimental and numerical curves of the recycled specimens in high strain rate conditions.

is well represented by the finite element models. The initial buckling behavior of the structures mainly depends on the yield values of the anisotropic model, thus proving that an accurate tuning is conducted. The uncertainty regarding the mechanical properties mainly comes from the plastic flow stress and failure parameters, which drive the behavior in the large strain regime (or plateau regime). Especially, failure parameters are to be properly evaluated from specific mechanical testing, which should be part of future work. However, numerical values are proven to be adequate for the representation of the behavior of the structures and can be used in the absence of experimental values.

Fig. 15 shows the comparison between the experimental and numerical collapse behavior, showing good accuracy in reproducing the buckling of the printed walls, as well as fracturing in the case of the 200 g/l. As discussed before, the equivalent strain at break is raised for 300 g/l and 400 g/l specimens, so that only limited fracturing occurs in the latest stages of compression. However, the collapse of the walls has the most important influence on the load-bearing behavior, as proved by the good reproduction of the load-displacement curves: even if less fracturing is observed in the finite element models, the accuracy is still preserved. The fracturing of the specimens occurs along the junction lines of internal walls with the external one, and this behavior is well captured by the finite element models (where severe bending deformation takes place). Figs. 16 and 17 show the comparison of experimental and numerical curves and collapse behaviors of the recycled 3D-printed specimens, respectively. The results show a good agreement between the experimental and numerical behaviors, with a maximum average error of 4.4% in terms of energy absorption for the 400 g/l specimen. As the behavior of the recycled specimens shows a greater effect of fracturing compared to pristine specimens, instantaneous errors in the load evaluation are more evident. As discussed, the energy absorption curves are less affected by this error due to spatial integration. Overall, peak loads and mean loads are well represented. The densification behavior is less evident due to fracturing, and the 400 g/l specimens show a greater discrepancy between the experimental and numerical results, due to the erosion criterion. Recycled specimens show a different fracturing behavior, which is again well captured by the finite element models. Walls printed junctions act as failure initiation points, driving the rupture of walls along their shared interfaces.

In conclusion, the material model presented herein is able to reproduce the experimental behavior of the anisotropic 3D-printed material. The main features of three different structures with two different materials (pristine and recycled) are well reproduced, showing good accuracy in terms of load and energy absorption values. The anisotropic modeling, along with the complete geometry reproduction, allows the design and verification of 3D-printed crash-absorbing structures, contributing to the extension of their use in engineering applications.

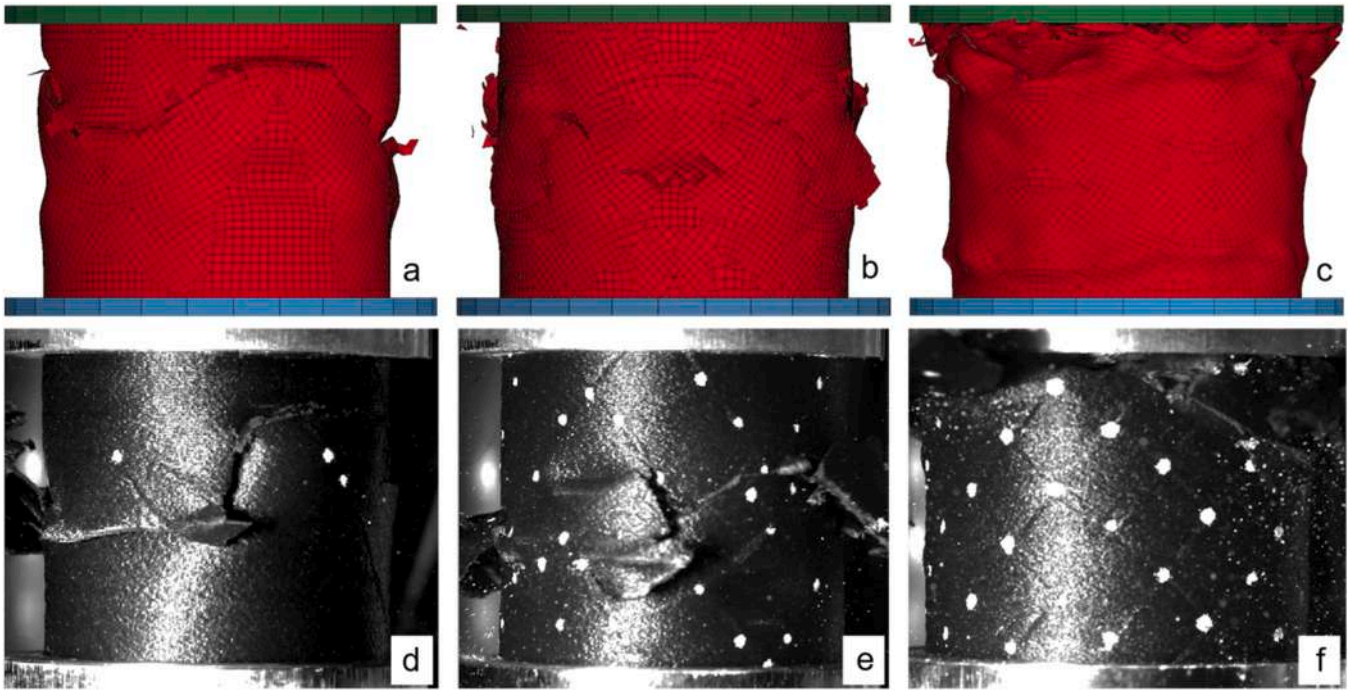

Fig. 17. Collapse behavior comparison between experimental tests and numerical simulations of recycled specimens.

5. Discussion

5.1. Typologies of lattice structures

3D-printed cellular structures have been demonstrated to be able to mitigate the effect of crash scenarios and impact loading. The increasing number of studies concentrating on the energy absorption performance of these types of structures denotes the rising interest in future applications in various engineering sectors. Automotive, aerospace, and packaging for shipping high-quality goods are only a few examples of the field of application of 3D-printed lattice structures. Their mechanical properties can be tuned based on the specific application, which allows for extending their possible usages. Different materials are used to fabricate lattice structures: among many, metal alloys and polymers are the most common ones. The first require higher technological levels in both raw material acquisition and production techniques, while the second allow reaching satisfying performances with lower investments.

Among different lattice structures, closed-cell and TPMS structures proved to be the better energy-absorbing ones [69]. This is due to their higher mechanical performances, given by their geometry: printed walls are more favourably oriented to support the load, and the cells are more interconnected to redistribute it efficiently, overcoming the stress concentration at nodes [70,71]. 2D lattices, although often providing negative Poisson's ratios, have a considerably high degree of anisotropy when tested in axial and transverse direction [72,73]. Truss lattices have generally lower mechanical properties and are more prone to defects during the manufacturing process, thus leading to early failure and less predictable mechanical properties [16,74]. Thus, when energy absorption properties and mechanical resistance are a priority, closed-cell and TPMS (or similar) lattice structures represent the optimal choice.

5.2. Strain rate effect on lattice structures

The mechanical performance of 3D-printed lattice structures is greatly affected by the effect of strain rate. According to many studies, the effect of impulse loading can be beneficial or detrimental, based on the material, structure, and printing technology employed. Some authors observed increased mechanical properties and energy absorption when testing specimens in high strain rate conditions, due to an increase in the mechanical properties of the base material. The latter condition, however, does not necessarily entail a beneficial effect of the strain rate on the final component, as observed by Bouteldja et al. [5]. Other authors observed a decrease in the energy absorption properties when passing from the quasi-static testing regime to the dynamic one, with embrittlement of the base material or with a complete change in the collapse dynamics. Analyzing the results available in the literature, one can conclude that no general law on the effect of the strain rate on 3D-printed structures has been found yet, and this is particularly true for polymeric ones. Accurate high strain rate testing is fundamental to determining the real crash absorption potential of 3D-printed lattice structures, and quasi-static tests can no longer be accepted alone. Before the mechanisms affecting the dynamic behavior of polymeric 3D-printed structures are clearly unraveled, dynamic testing is a critical step that future work must address.

5.3. DIHPB with wave separation technique

Compared to a typical drop tower test, where load and displacement are not directly measured, the DIHPB apparatus allows for improved results and accurate evaluation of the crashworthiness properties. The wave separation technique with the deconvolution method removes the need for a sufficiently long output bar, as the stress wave is allowed to superimpose itself without precluding the analysis. This means that, properly accounting for dispersion effects, a very short output bar can be employed, with no theoretical limitation. The only additional requirements for the development of this setup are: the knowledge of the wave speed function (depending on the wave component frequency), the installation of at least two strain gages, and the knowledge of the mathematical operations needed to separate the waves. Furthermore, the more strain gages are used, the more accurate the separated signal will be. The addition of line scan cameras allows for the accurate measurement of displacement and the fine calibration of strain gages in high-speed conditions.

5.4. Recycled polymers for engineering components

Recent interest in the recycling of plastics through 3D printing techniques has posed the challenge of finding engineering solutions for recycled products. The effect of the mechanical recycling process through additive manufacturing is not yet completely clear, while some engineering components are already found in some commercial applications. Mostly, recycled materials are downcycled to non-structural components, losing a major part of their initial value. The effects of the recycling process on the mechanical performance of 3D-printed materials have been recently investigated, showing that multiple regrinding and reprinting of specimens affect their mechanical properties, as expected. Hence, the aim of research should be to find solutions to mitigate the impact of the deteriorating mechanisms acting during the operating life and recycling process of components.

The sole mechanical characterization of the base material with conventional tensile testing could be insufficient to predict the behavior of 3D-printed structures. Especially when dealing with energy-absorbing structures, complex deformation and loading of the material occur, which is further complicated by the effect of strain rate. Hence, some aspects are not captured until experimental testing is conducted on the final components. As an example, the role of the base material density is highlighted in the present work, showing how a theoretically stronger material can result in lower energy absorption properties of the built structure. FGF printing, used to directly process recycled polymers, reduces the porosity of the material due to the different material processing conditions compared to FFF printing. As a possible solution to this problem, foaming agents could be employed to introduce a controlled degree of porosity and increase the compliance of the printed walls to large bending deformation [60–63].

Summary and conclusion

The present work investigates the crashworthiness of 3D-printed fiber-reinforced polymeric pristine and recycled lattice structures, printed with different overall densities of 200 g/l, 300 g/l, and 400 g/l. The main energy absorption parameters are evaluated both in quasi-static and dynamic conditions to evaluate their performances and investigate the effect of strain rate. An advanced DIHPB setup is employed to test the 3D-printed structures at high strain rate, using a wave separation technique that allows for the testing of large displacements without the need for a prohibitively long output bar. Three strain gage stations are used to separate the wave through a deconvolution technique, while line scan cameras are used for the calibration and verification of the strain gages' signals. High-speed cameras are employed to record the displacements of the striker and the bar, as well as the collapse behavior of the specimens. Lastly, finite element models are developed to be used as design and verification tools for the development of future engineering applications. The same anisotropic material model is used to simulate both the pristine and recycled materials, adjusting the failure properties to represent the reduced strain at break observed for the recycled material.

The main findings of the present work can be summarized as follows:

- Recycled 3D-printed fiber-reinforced lattice structures proved higher mechanical performances than their pristine counterparts in quasi-static conditions. The reason for this mainly lies in the different printing technique, which has been previously proven by the authors to introduce relevant changes in the microstructure of the base material. The porosity of the material is crucial to determining its mechanical properties and its ability to withstand deformation in dynamic conditions: a higher degree of porosity helps the material with a more cushioning and compliant behavior. The recycled one is printed by FGF printing, while the pristine one is printed by FFF printing, resulting in a higher porosity. The recycled material produced by FGF printing has higher mechanical properties, which result in higher energy absorption of the structures.
- The mechanical behavior of all 3D-printed structures is influenced by the overall density. Not only energy-absorption properties, but also collapse mechanisms are affected by the density, which directly influences the geometry of the structures.
- The behavior of both 3D-printed lattices is greatly influenced by strain rate: both materials experience embrittlement and higher mechanical properties as loads increase and failures are observed. Pristine specimens experience a positive influence of the strain rate, with an increase in SEA up to 22% for the 400 g/l specimens (from 10.79 J/g to 13.21 J/g). Recycled specimens experience catastrophic collapse and failure, showing decreases in SEA up to 25% for the 300 g/l specimens (from 9.50 J/g to 7.10 J/g). These results prove that the dynamic behavior of lattice structures must be evaluated carefully, and quasi-static tests are not adequate alone.
- The anisotropic material model developed in the present work is able to correctly reproduce the main features of the mechanical behavior of the structures, both in terms of overall properties and collapse mechanisms. The anisotropic nature of the 3D-printed structures is particularly evident at lower densities, where the limited number of cells localizes the bending and failure behaviors. This modeling strategy proves to be accurate for the future development of design and structural verification analyses.

The present work is, to the best of the authors' knowledge, the first to investigate the crashworthiness of recycled 3D-printed structures. The need for recycling plastics is rising, and further research is needed to assess the possible applications for recycled polymers in the additive manufacturing industry. Future work should be directed to widen the choice of recycled polymers employed to build functional components, possibly aiming for low-value plastics coming from the urban recycling sector, as well as high-end composites, which are difficult to recycle conventionally. Further research efforts will increase the possibility of limiting downcycling and exploring upcycling paths.

CRediT authorship contribution statement

Martina Scapin: Writing – review & editing, Validation, Supervision, Project administration, Methodology, Investigation, Funding acquisition, Conceptualization. **Lorenzo Peroni:** Writing – review & editing, Validation, Supervision, Software, Methodology, Investigation, Funding acquisition, Conceptualization. **Francesco Bandinelli:** Writing – review & editing, Writing – original draft, Visualization, Validation, Software, Methodology, Investigation, Formal analysis, Data curation, Conceptualization.

Declaration of Competing Interest

The authors declare that they have no known competing financial interests or personal relationships that could have appeared to influence the work reported in this paper.

Data availability

Data will be made available on request.

References

[1] Y. Wu, J. Fang, C. Wu, C. Li, G. Sun, Q. Li, Additively manufactured materials and structures: A state-of-the-art review on their mechanical characteristics and energy absorption, Elsevier Ltd,, May 15, 2023, https://doi.org/10.1016/j.ijmecsci.2023.108102.

[2] J. Zhang, G. Lu, Z. You, Large deformation and energy absorption of additively manufactured auxetic materials and structures: A review, Elsevier Ltd,, Nov. 15, 2020, https://doi.org/10.1016/j.compositesb.2020.108340.

[3] H. Yin, W. Zhang, L. Zhu, F. Meng, J. Liu, G. Wen, Review on lattice structures for energy absorption properties, Elsevier Ltd,, Jan. 15, 2023, https://doi.org/10.1016/j.compstruct.2022.116397.

[4] R. Santiago, et al., Modelling and optimisation of TPMS-based lattices subjected to high strain-rate impact loadings, Int. J. Impact Eng. 177 (Jul. 2023), https://doi.org/10.1016/j.ijimpeng.2023.104592.

[5] A. Bouteldja, M.A. Louar, L. Hemmouche, L. Gilson, A. Miranda-Vicario, L. Rabet, Experimental investigation of the quasi-static and dynamic compressive behavior of polymer-based 3D-printed lattice structures, Int. J. Impact Eng. 180 (Oct. 2023), https://doi.org/10.1016/j.ijimpeng.2023.104640.

[6] S.E. Alkhatib, A. Karrech, T.B. Sercombe, Isotropic energy absorption of topology optimized lattice structure, Thin-Walled Struct. 182 (Jan. 2023), https://doi.org/10.1016/j.tws.2022.110220.

[7] C. Peng, P. Tran, A.P. Mouritz, Compression and buckling analysis of 3D printed carbon fibre-reinforced polymer cellular composite structures, Compos. Struct. 300 (Nov. 2022), https://doi.org/10.1016/j.compstruct.2022.116167.

[8] C.B. Niutta, R. Ciardiello, A. Tridello, Experimental and numerical investigation of a lattice structure for energy absorption: application to the design of an automotive crash absorber, Polymers 14 (6) (Mar. 2022), https://doi.org/10.3390/polym14061116.

[9] J.J. Andrew, H. Alhashmi, A. Schiffer, S. Kumar, V.S. Deshpande, Energy absorption and self-sensing performance of 3D printed CF/PEEK cellular composites, Mater. Des. 208 (Oct. 2021), https://doi.org/10.1016/j.matdes.2021.109863.

[10] Y. Duan, et al., Effects of cell size vs. cell-wall thickness gradients on compressive behavior of additively manufactured foams, Compos. Sci. Technol. 199 (Oct. 2020), https://doi.org/10.1016/j.compscitech.2020.108339.

[11] G. Feng, S. Li, L. Xiao, W. Song, Mechanical properties and deformation behavior of functionally graded TPMS structures under static and dynamic loading, Int. J. Impact Eng. 176 (Apr. 2023), https://doi.org/10.1016/j.ijimpeng.2023.104554.

[12] S. AlMahri, et al., Evaluation of the dynamic response of triply periodic minimal surfaces subjected to high strain-rate compression, Addit. Manuf. 46 (Oct. 2021), https://doi.org/10.1016/j.addma.2021.102220.

[13] C.R. Calladine, R.W. English, Strain-rate and inertia effects in the collapse of two types of energy-absorbing structure, Int. J. Mech. Sci. 26 (11) (1984) 689–701.

[14] I. Elnasri, S. Pattofatto, H. Zhao, H. Tsitsiris, F. Hild, Y. Girard, Shock enhancement of cellular structures under impact loading: Part I Experiments, J. Mech. Phys. Solids 55 (12) (Dec. 2007) 2652–2671, https://doi.org/10.1016/j.jmps.2007.04.005.

[15] D.W. Abueidda, M. Elhebeary, C.S. (Andrew) Shiang, S. Pang, R.K. Abu Al-Rub, I. M. Jasiuk, Mechanical properties of 3D printed polymeric Gyroid cellular structures: Experimental and finite element study, Mater. Des. 165 (Mar. 2019), https://doi.org/10.1016/j.matdes.2019.107597.

[16] R. Nam, M. Jakubinek, H. Niknam, M. Rahmat, B. Ashrafi, H.E. Naguib, 3D printed octet plate-lattices for tunable energy absorption, Mater. Des. 228 (Apr. 2023), https://doi.org/10.1016/j.matdes.2023.111835.

[17] N. Kladovasilakis, K. Tsongas, I. Kostavelis, D. Tzovaras, D. Tzetzis, Effective mechanical properties of additive manufactured triply periodic minimal surfaces: experimental and finite element study, Int. J. Adv. Manuf. Technol. 121 (11–12) (Aug. 2022) 7169–7189, https://doi.org/10.1007/s00170-022-09651-w.

[18] J.S. Weeks, G. Ravichandran, High strain-rate compression behavior of polymeric rod and plate Kelvin lattice structures, Mech. Mater. 166 (Mar. 2022), https://doi.org/10.1016/j.mechmat.2022.104216.

[19] J. Allum, A. Gleadall, V.V. Silberschmidt, Fracture of 3D-printed polymers: crucial role of filament-scale geometric features, Eng. Fract. Mech. 224 (Feb. 2020), https://doi.org/10.1016/j.engfracmech.2019.106818.

[20] United Nations Environment Programme, Turning off the tap. How the world can end plastic pollution and create a circular economy, United Nations Environment Programme,, Nairobi, 2023.

[21] H.A. Colorado, E.I.G. VelÁsquez, S.N. Monteiro, Sustainability of additive manufacturing: the circular economy of materials and environmental perspectives, J. Mater. Res. Technol. 9 (4) (Jul. 2020) 8221–8234, https://doi.org/10.1016/j.jmrt.2020.04.062.

[22] M. Hassan, A.K. Mohanty, M. Misra, 3D printing in upcycling plastic and biomass waste to sustainable polymer blends and composites: a review, Elsevier Ltd,, Jan. 01, 2024, https://doi.org/10.1016/j.matdes.2023.112558.

[23] F.A. Cruz Sanchez, H. Boudaoud, S. Hoppe, M. Camargo, Polymer recycling in an open-source additive manufacturing context: mechanical issues, Addit. Manuf. 17 (Oct. 2017) 87–105, https://doi.org/10.1016/j.addma.2017.05.013.

[24] A. Spirio, R. Arrigo, A. Frache, L. Tuccinardi, R. Tuffi, Plastic waste recycling in additive manufacturing: recovery of polypropylene from WEEE for the production of 3D printing filaments, J. Environ. Chem. Eng. 12 (3) (Jun. 2024), https://doi.org/10.1016/j.jece.2024.112474.

[25] R. Walker, et al., Recycling of CF-ABS machining waste for large format additive manufacturing, Compos. B Eng. 275 (Apr. 2024), https://doi.org/10.1016/j.compositesb.2024.111291.

[26] W. Ma, Q. Dong, H. Zhao, X. Li, L. Xiong, N. Hu, Mechanics-guided manufacturing optimization framework to enhance the strength of architected lattice made from recycled plastic wastes, Addit. Manuf. 81 (Feb. 2024), https://doi.org/10.1016/j.addma.2024.103997.

[27] F. Bandinelli, E. Tito, E. Parisi, L. Peroni, M. Scapin, Recycling a carbon fiber-reinforced polyamide through 3D printing: a mechanical and physicochemical analysis, Compos. B Eng. 294 (Apr. 2025), https://doi.org/10.1016/j.compositesb.2025.112147.

[28] D.J. Byard, A.L. Woern, R.B. Oakley, M.J. Fiedler, S.L. Snabes, J.M. Pearce, Green fab lab applications of large-area waste polymer-based additive manufacturing, Addit. Manuf. 27 (May 2019) 515–525, https://doi.org/10.1016/j.addma.2019.03.006.

[29] H. Li, et al., Interlayer enhancement of 3D printed CF/PLA composites via localized microwave welding and annealing-induced crystallization, Compos. B Eng. 284 (Sep. 2024), https://doi.org/10.1016/j.compositesb.2024.111737.

[30] R. Hashemi Sanatgar, C. Campagne, V. Nierstrasz, Investigation of the adhesion properties of direct 3D printing of polymers and nanocomposites on textiles: Effect of FDM printing process parameters, Appl. Surf. Sci. 403 (May 2017) 551–563, https://doi.org/10.1016/j.apsusc.2017.01.112.

[31] F. Bandinelli, M. Scapin, L. Peroni, High strain rate testing and modeling of 3D-printed polymeric cellular structures, Thin-Walled Struct. 218 (Jan. 2026), https://doi.org/10.1016/j.tws.2025.114081.

[32] P. Kumar A, Q. Ma, Evaluation of energy absorption enhancement of additively manufactured polymer composite lattice structures, Funct. Compos. Struct. 5 (1) (Mar. 2023), https://doi.org/10.1088/2631-6331/acc0d0.

[33] M.M. Rahman, J. Sultana, S.Bin Rayhan, A. Ahmed, Optimization of FDM manufacturing parameters for the compressive behavior of cubic lattice cores: an experimental approach by Taguchi method, Int. J. Adv. Manuf. Technol. 129 (3–4) (Nov. 2023) 1329–1343, https://doi.org/10.1007/s00170-023-12342-9.

[34] A. Romani, L. Perusin, M. Ciurnelli, M. Levi, Characterization of PLA feedstock after multiple recycling processes for large-format material extrusion additive manufacturing, Mater. Today Sustain. 25 (Mar. 2024), https://doi.org/10.1016/j.mtsust.2023.100636.

[35] F. Bandinelli, A. Ciampaglia, R. Ciardiello, L. Peroni, M. Peroni, M. Scapin, High strain rate testing of carbon-epoxy laminate crash boxes filled with polymeric cellular 3D-printed cores, Int. J. Impact Eng. 205 (Nov. 2025), https://doi.org/10.1016/j.ijimpeng.2025.105401.

[36] J. Shim, D. Mohr, Using split Hopkinson pressure bars to perform large strain compression tests on polyurea at low, intermediate and high strain rates, Int. J. Impact Eng. 36 (9) (2009) 1116–1127, https://doi.org/10.1016/j.ijimpeng.2008.12.010.

[37] T. FÍla, J. Falta, R. DvořÁk, A simple wave separation method for Split Hopkinson Bar experiments using linear encoders, Results Eng. 28 (Dec. 2025) 106980, https://doi.org/10.1016/j.rineng.2025.106980.

[38] M. Peroni, G. Solomos, N. Babcsan, Development of a Hopkinson bar apparatus for testing soft materials: application to a closed-cell aluminum foam, Materials 9 (1) (2016), https://doi.org/10.3390/ma9010027.

[39] M.-N.E. Bussac, P. Collet, E. Gary, and R. Othman, "An optimisation method for separating and rebuilding one-dimensional dispersive waves from multi-point measurements. Application to elastic or viscoelastic bars," 2002. [Online]. Available: ⟨www.elsevier.com/locate/jmps⟩.

[40] L. Pochhammer Von Herrn, "Ueber die Fortpflanzungsgeschwindigkeiten kleiner Schwingungenin einem unbegrenzten isotropen Kreiscylinder,", J. Reine Angew. Math. 81 (1876).

[41] Z. Li, T.X. Yu, L. Wan, Q. Zeng, D. Ruan, Non-dimensional parameters governing the crashworthy performance of tubes with complex cross-sections, Int. J. Mech. Sci. 278 (Oct. 2024), https://doi.org/10.1016/j.ijmecsci.2024.109476.

[42] Y. Xiang, T. Yu, L. Yang, Comparative analysis of energy absorption capacity of polygonal tubes, multi-cell tubes and honeycombs by utilizing key performance indicators, Mater. Des. 89 (Jan. 2016) 689–696, https://doi.org/10.1016/j.matdes.2015.10.004.

[43] P. Wang, et al., Anisotropic compression behaviors of bio-inspired modified body-centered cubic lattices validated by additive manufacturing, Compos. B Eng. 234 (Apr. 2022), https://doi.org/10.1016/j.compositesb.2022.109724.

[44] X. Liu, B. Chi, Z. Jiao, J. Tan, F. Liu, W. Yang, A large-scale double-stage-screw 3D printer for fused deposition of plastic pellets, J. Appl. Polym. Sci. 134 (31) (Aug. 2017), https://doi.org/10.1002/app.45147.

[45] P.K. Penumakala, J. Santo, A. Thomas, A critical review on the fused deposition modeling of thermoplastic polymer composites, Nov. 15, Elsevier Ltd,, 2020, https://doi.org/10.1016/j.compositesb.2020.108336.

[46] Y. Cheng, Y. Li, X. Chen, X. Zhou, N. Wang, Compressive properties and energy absorption of aluminum foams with a wide range of relative densities, J. Mater. Eng. Perform. 27 (8) (Aug. 2018) 4016–4024, https://doi.org/10.1007/s11665-018-3514-4.

[47] Y. Wang, et al., Micro-CT in the mechanical properties and energy absorption of closed-cell aluminium foam, Mater. Today Commun. 37 (Dec. 2023), https://doi.org/10.1016/j.mtcomm.2023.106962.

[48] Y. Duan, B. Du, X. Shi, B. Hou, Y. Li, Quasi-static and dynamic compressive properties and deformation mechanisms of 3D printed polymeric cellular structures with Kelvin cells, Int. J. Impact Eng. 132 (Oct. 2019), https://doi.org/10.1016/j.ijimpeng.2019.05.017.

[49] C. Quan, B. Han, Z. Hou, Q. Zhang, X. Tian, T.J. Lu, 3d printed continuous fiber reinforced composite auxetic honeycomb structures, Compos. B Eng. 187 (Apr. 2020), https://doi.org/10.1016/j.compositesb.2020.107858.

[50] Z.P. Sun, Y.B. Guo, V.P.W. Shim, Characterisation and modeling of additively-manufactured polymeric hybrid lattice structures for energy absorption, Int. J. Mech. Sci. 191 (Feb. 2021), https://doi.org/10.1016/j.ijmecsci.2020.106101.

[51] F.H. ÖztÜrk, İ.A. Karamanlı, A. Temiz, Strut-based design optimization for improving mechanical properties of lattice structures, Int. J. Mech. Mater. Des. 21 (3) (Jun. 2025) 591–608, https://doi.org/10.1007/s10999-025-09751-x.

[52] Z. Zhang, K. Wang, B.A. Bednarcyk, L. Le Barbenchon, Y. Chen, Tailoring the architecture of fractal lattice metamaterials for tunable energy absorption, Compos. B Eng. 305 (Oct. 2025), https://doi.org/10.1016/j.compositesb.2025.112711.

[53] T. Fisher, J.H.S. Almeida, B.G. Falzon, Z. Kazancı, Tension and compression properties of 3D-printed composites: print orientation and strain rate effects, Polymers 15 (7) (Apr. 2023), https://doi.org/10.3390/polym15071708.
[54] K. Wang, et al., Materials selection of 3D printed polyamide-based composites at different strain rates: a case study of automobile front bumpers, J. Manuf. Process 84 (Dec. 2022) 1449–1462, https://doi.org/10.1016/j.jmapro.2022.11.024.
[55] X. Yang, L.G. Hector, J. Wang, A combined theoretical/experimental approach for reducing ringing artifacts in low dynamic testing with servo-hydraulic load frames, Exp. Mech. 54 (5) (2014) 775–789, https://doi.org/10.1007/s11340-014-9850-x.
[56] Y. Xu, G. Quino, K.R. Ramakrishnan, A. Pellegrino, Effects of build orientation and strain rate on the tensile-shear behaviour of polyamide-12 manufactured via laser powder bed fusion, Mater. Des. 232 (Aug. 2023), https://doi.org/10.1016/j.matdes.2023.112162.
[57] R. Balieu, et al., Damage at high strain rates in semi-crystalline polymers, Int. J. Impact Eng. 76 (2015) 1–8, https://doi.org/10.1016/j.ijimpeng.2014.08.013.
[58] Z. Zhuang, et al., Bioinspired structural composite flexible material with high cushion performance, Adv. Sci. 11 (5) (Feb. 2024), https://doi.org/10.1002/advs.202304947.
[59] H.Bin Yang, et al., Multiscale integral synchronous assembly of cuttlebone-inspired structural materials by predesigned hydrogels, Nat. Commun. 16 (1) (Dec. 2025), https://doi.org/10.1038/s41467-024-55344-1.
[60] X. Liu, et al., 4D printing of cellular silicones with negative stiffness effect for enhanced energy absorption and impact protection, Compos. B Eng. 282 (Aug. 2024), https://doi.org/10.1016/j.compositesb.2024.111561.
[61] Q. Liu, L. Hong, X. Dong, W. Zhai, 3D printed hierarchical interpenetrating phase composites with multi-scale mechanical energy absorption mechanisms, Compos. B Eng. 264 (Sep. 2023), https://doi.org/10.1016/j.compositesb.2023.110911.
[62] Y. Kwon, et al., 3D-printed polymer foams maintain stiffness and energy dissipation under repeated loading, Compos. Commun. 37 (Jan. 2023), https://doi.org/10.1016/j.coco.2022.101453.
[63] S. Zhang, et al., 3D-printed multiscale hierarchical thermoplastic polyurethane/aramid nanofiber structures with enhanced energy absorption via in-Situ foaming technology, Virtual Phys. Prototyp. 20 (1) (2025), https://doi.org/10.1080/17452759.2025.2558972.
[64] G. Sun, S. Li, Q. Liu, G. Li, Q. Li, Experimental study on crashworthiness of empty/aluminum foam/honeycomb-filled CFRP tubes, Compos. Struct. 152 (Sep. 2016) 969–993, https://doi.org/10.1016/j.compstruct.2016.06.019.
[65] W. Song, R. Li, G. Feng, L. Xiao, Dynamic mechanical behaviors and deformation mechanism of hybrid triply periodic minimal surface structures, Int. J. Impact Eng. 203 (Sep. 2025), https://doi.org/10.1016/j.ijimpeng.2025.105359.
[66] F. Bandinelli, L. Peroni, A. Morena, Elasto-plastic mechanical modeling of fused deposition 3D printing materials, Polym. (Basel) 15 (1) (Jan. 2023), https://doi.org/10.3390/polym15010234.
[67] F. Bandinelli, M. Scapin, L. Peroni, Effects of anisotropy and infill pattern on compression properties of 3D printed CFRP: mechanical analysis and elasto-plastic finite element modelling, Rapid Prototyp. J. 30 (11) (2024) 142–158, https://doi.org/10.1108/RPJ-11-2023-0385.
[68] R.B. Colby, Equivalent plastic strain for the hill's yield criterion under general three-dimensional loading author, Accessed: Nov. 28, Mass. Inst. Technol. 2013 (2025). Accessed: Nov. 28, ⟨http://hdl.handle.net/1721.1/83690⟩.
[69] Z. Yu, R. Savinov, M. Matura, P. Zhang, J. Shi, Current research status on advanced lattice structures for impact and energy absorption applications: a systematic review, Elsevier Ltd,, Oct. 01, 2025, https://doi.org/10.1016/j.tws.2025.113490.
[70] J.B. Berger, H.N.G. Wadley, R.M. McMeeking, Mechanical metamaterials at the theoretical limit of isotropic elastic stiffness, Nature 543 (7646) (Mar. 2017) 533–537, https://doi.org/10.1038/nature21075.
[71] M. Ghosh, et al., Scalability in SLA lattice through lattice orientation and hybrid frame and plate architectures, J. Mater. Res. Technol. 35 (Mar. 2025) 645–659, https://doi.org/10.1016/j.jmrt.2024.12.155.
[72] C. Zeng, L. Liu, W. Bian, J. Leng, Y. Liu, Compression behavior and energy absorption of 3D printed continuous fiber reinforced composite honeycomb structures with shape memory effects, Addit. Manuf. 38 (Feb. 2021), https://doi.org/10.1016/j.addma.2021.101842.
[73] M.K. Khan, T. Baig, S. Mirza, Experimental investigation of in-plane and out-of-plane crushing of aluminum honeycomb, Mater. Sci. Eng. A 539 (Mar. 2012) 135–142, https://doi.org/10.1016/j.msea.2012.01.070.
[74] Z. Liu, H. Chen, S. Xing, Mechanical performances of metal-polymer sandwich structures with 3D-printed lattice cores subjected to bending load, Arch. Civ. Mech. Eng. 20 (3) (Sep. 2020), https://doi.org/10.1007/s43452-020-00095-1.